Shock Layer Radiation Modeling and Uncertainty for Mars Entry

Christopher O. Johnston,[*]

NASA Langley Research Center, Hampton, VA 23681

Aaron M. Brandis[†]

University Affiliated Research Center with University of California Santa Cruz,

Mountain View, CA 94035

and

Kenneth Sutton[‡]

National Institute of Aerospace, Hampton, VA 23669

A model for simulating nonequilibrium radiation from Mars entry shock layers is presented. A new chemical kinetic rate model is developed that provides good agreement with recent EAST and X2 shock tube radiation measurements. This model includes a CO dissociation rate that is a factor of 13 larger than the rate used widely in previous models. Uncertainties in the proposed rates are assessed along with uncertainties in translational-vibrational relaxation modeling parameters. The stagnation point radiative flux uncertainty due to these flowfield modeling parameter uncertainties is computed to vary from 50 to 200% for a range of free-stream conditions, with densities ranging from 5e-5 to 5e-4 kg/m^3 and velocities ranging from of 6.3 to 7.7 km/s. These conditions cover the range of anticipated peak radiative heating conditions for proposed hypersonic inflatable aerodynamic decelerators (HIADs). Modeling parameters for the radiative spectrum are compiled along with a non-Boltzmann rate model for the dominant radiating molecules, CO, CN, and C_2. A method for treating non-local absorption in the non-Boltzmann model is developed, which is shown to result in up to a 50% increase in the radiative flux through absorption by the CO 4th Positive band. The sensitivity of the radiative flux to the radiation modeling parameters is presented and the uncertainty for each parameter is assessed. The stagnation point radiative flux uncertainty due to these radiation modeling parameter uncertainties is computed to vary from 18 to 167% for the considered range of free-stream conditions. The total radiative flux uncertainty is computed as the root sum square of the flowfield and radiation parametric uncertainties, which results in total uncertainties ranging from 50 to 260%. The main contributors to these significant uncertainties are the CO dissociation rate and the CO heavy-particle excitation rates. Applying the baseline flowfield and radiation models developed in this work, the radiative heating for the Mars Pathfinder probe is predicted to be nearly 20 W/cm^2. In contrast to previous studies, this value is shown to be significant relative to the convective heating.

I. Nomenclature

$A_{v'v''}$ — Einstein emission coefficient for a vibrational-electronic transition (s^{-1})
$A_{f,i}$ — Leading rate constant for chemical kinetic reaction i
B_v — Spectroscopic constant for rotational energy (cm^{-1})
$C_{v,v}$ — Specific heat at constant volume for vibrational-electronic energy (J/kg/K)
c — Speed of light, 2.9979×10^{10} cm/s

---

[*]Aerospace Engineer, Aerothermodynamics Branch, Research Directorate, AIAA Member.
[†]Associate Research Scientist, AIAA Professional Member
[‡]Research Scientist, AIAA Associate Fellow

$D_{f,i}$	Characteristic temperature for chemical kinetic rate constant i (K)
E_v	Vibrational energy (cm^{-1})
E_e	Electronic energy (cm^{-1})
E_2	Second-order exponential integral
G_{ab}	Radiative absorption term defined in text ($particles - s^{-1} - cm^{-3}$)
F_i	Baseline rate divided by heritage rate at 8000 K.
G_{em}	Radiative lifetime defined in text (s^{-1})
g_e	Electronic degeneracy
h	Planck's constant, 6.6256×10^{-27} erg-s
I_ν	Frequency-dependent intensity resulting from all radiative mechanisms (W/cm^2/sr)
J_λ	Frequency-dependent intensity divided by shock tube diameter (W/cm^3/sr/μ)
J_c	Integrated intensity divided by shock tube diameter (W/cm^3/sr)
$j_{\nu,ij}$	Frequency-dependent emission coefficient for transition between electronic levels i and j (erg/cm^3/sr)
k	Boltzmann constant, 1.3806×10^{-16} erg/K
$k_{f,i}$	Forward rate for chemical reaction i (cm^{3}mole^{-1}s^{-1})
$k_{b,i}$	Backward rate for chemical reaction i (cm^{3}mole^{-1}s^{-1})
K_r	Reaction rate constant for reaction r (K)
N_j	Number density of electronic level j (particles/cm^3)
$n_{f,i}$	Temperature exponent for chemical kinetic reaction i
q_r	Radiative flux at the wall (W/cm^2)
$q_{r,upper}$	Radiative flux at the wall multiplied by the positive component of $\Delta q_{r,total}$ (W/cm^2)
Q_e	Electronic partition function
Q_{int}	Internal partition function
Q_{v-t}	Vibrational-translational relaxation term (J/m^3/s)
R_ν	Blackbody function (erg-cm^{-2}-sr)
s	Integration variable
T_a	Dissociation controlling average temperature defined as $(T_{tr}T_{ve})^{1/2}$ (K)
T_x	Temperature, where $x=e,v$, or r for electronic, vibrational, or rotational modes (K)
z	Distance along a body normal (cm)
$\Delta q_{r,flow}$	Radiative flux uncertainty due to flowfield modeling parameters
$\Delta q_{r,rad}$	Radiative flux uncertainty due to radiation modeling parameters
$\Delta q_{r,total}$	Total radiative flux uncertainty, computed as the root sum square of $\Delta q_{r,flow}$ and $\Delta q_{r,rad}$
$\kappa_{\nu,ij}$	Absorption coefficient including induced emission for transition between electronic levels i and j (cm^{-1})
λ	wavelength (nm)
$\Lambda_{j,i}$	Escape factor (dimensionless)
μ	Reduced mass between colliding species
ν	Frequency (s^{-1})
Ψ	Solid angle
ρ_{inf}	Free stream density (kg/m^3)
τ_ν	Optical depth (dimensionless)

II.   Introduction

The influence of radiative heating on the aerothermal environment of future NASA missions to Mars is potentially significant.[1] Concepts such as hypersonic inflatable aerodynamic decelerators (HIADs)[2] may consist of a geometry similar to a 70 degree sphere cone with a diameter as large as 20 m. This large diameter will result in radiative heating that is a significant fraction of the convective heating, if not larger. Proposed materials for the inflatable structure have relatively low heat flux limits ($\sim$40 W/cm^2). The accurate prediction of the radiative and convective heating at these low magnitudes, which will likely occur at high altitudes with strong shock-layer thermochemical nonequilibrium, presents a significant challenge for NASA's present aerothermodynamic simulation capability. Hollis and Prabhu[3] reviewed the state-of-the-art simulation capability for *convective* heating of a Mars entry vehicle. The focus of the present paper is to define a baseline simulation approach for Mars entry *radiative* heating predictions and to assess the uncertainty associated with this baseline model.

The chemical kinetic and two-temperature modeling parameters presented in 1994 by Park et al.[4] have been the standard at NASA during the past two decades for Mars entry flowfield simulations. Because of the relatively low entry velocities (<6 km/s) of Mars missions during this time[1] (with the exception of Mars Pathfinder), the majority of Mars entry simulations using the Park model have been focused on accurate convective heating predictions, which are significantly less sensitive to the chemical kinetic and two-temperature modeling parameters than the radiative heating (the convective heating being most sensitive to the catalycity model). Many comparisons with convective heating measurements have been performed to assess this model for convective heating predictions.[3] Although some comparisons with radiation measurements have been made recently using this model,[5–10] the experimental conditions were far from flight relevant and the main radiating band system, the CO 4th Positive band, was not measured. Recent measurements by Cruden et al.[11] in the NASA Ames EAST facility have provided measurements of the CO 4th Positive and CN Violet bands at pressures and velocities relevant to HIAD entries. These measurements, along with recent theoretical studies of Mars entry flowfield and radiation properties,[12–16] provide an opportunity to assess the radiative heating prediction capability of the Park model[4] and to make adjustments where necessary. These tasks are the goal of the present paper, which will develop a chemical kinetic rate model by tuning the Park model to fit the EAST measurements, and will develop radiative spectrum and non-Boltzmann models based on recent data from the literature. Furthermore, the radiative heating uncertainty for these developed models will be assessed through a parametric uncertainty analysis, using uncertainties for each modeling parameter chosen during model development.

A brief overview of the flowfield and radiation codes used to implement the developed models is presented in Section III. The flowfield conditions and geometry of present interest are also defined in this section, along with an overview of shock layer radiative heating for HIADs entering Mars. Section IV presents the modifications made to the Park et al.[4] chemical kinetics for the present baseline model. The rates are tuned to provide good agreement with recent EAST shock tube measurements by Cruden et al.[11] Section V presents a sensitivity analysis of the radiative heating to this new rate model and the vibrational relaxation model. Uncertainties for the rates and relaxation parameters are chosen based on a literature review, and a parametric radiative heating uncertainty is computed based on these flowfield modeling uncertainties. Section VI presents the baseline radiation model, which includes spectrum and non-Boltzmann modeling parameters. Uncertainties for these parameters are chosen based on a literature review, and a parametric radiative heating uncertainty is computed based on these radiation modeling uncertainties. Section VII combines the flowfield and radiation modeling parametric uncertainties from Sections V and VI and discusses the total radiative heating uncertainty for Mars entry. Finally, Section VIII applies the developed radiation model and uncertainty approach to the Mars Pathfinder vehicle.

III.   Mars Entry Radiation Overview

This section provides an overview of the flowfield and radiation codes applied in this work, along with the vehicle geometry and range of free-stream conditions considered. Radiative heating results are also presented to provide a general overview of the nonequilibrium shock layers present at these conditions.

A.   Overview of Applied Flowfield and Radiation Codes

The present baseline flowfield model is implemented using the LAURA Navier-Stokes solver.[17] As mentioned in the Introduction, the two-temperature thermochemical nonequilibrium model presented by Park et al.[4] is applied in this work, with chemical rate modifications made based on comparisons with shock tube radiation measurements. These modified rates will be presented in Section IV, while details of the two-temperature formulation are presented in Section V with the discussion of flowfield uncertainties. The following 16 species are treated: CO_2, CO, N_2, O_2, NO, C, N, O, CN, C_2, C^+, O^+, NO^+, O_2^+, CO^+, and e^-. Note that although NCO was included by Park et al.,[4] it is ignored throughout this work because its impact on radiative and convective heating was found to be negligible.

The present baseline radiation model is implemented using the HARA nonequilibrium radiation code[18, 19] with tangent-slab radiation transport. Emission and absorption from C, O, and N species are treated, which includes bound-free (photoionization), free-free, and bound-bound (atomic lines) radiative processes. The computational approach and spectral data applied for modeling these processes are presented by Johnston.[20] Note that the contribution from these atomic species is less than 3% of the total radiative flux for the Mars

entry conditions of present interest.

The major contributors to Mars entry radiation are the molecular band systems, particularly the CO 4th Positive, CN Violet, CN Red, and C_2 Swan bands. A complete list of the band systems treated and the parameters used for their modeling is presented in Section VI. The strong CO 4th Positive band emits in the vacuum ultraviolet region of the spectrum, and therefore experiences significant self absorption for most shock layer conditions. This optically thick molecular band system requires the use of the rigorous line-by-line (LBL) approach for radiation transport, instead of the more efficient smeared rotational band approach previously applied by HARA.[18] The option to treat specified band systems using the LBL approach, while simultaneously treating other weaker bands systems using the SRB approach, was recently implemented in HARA and will be applied throughout this work. It was found that only the CO 4th Positive band requires the LBL approach for flight cases. Validation of the present LBL simulation for the CO 4th Positive band is presented by Brandis et al.[21]

B.   Baseline Geometry and Free-Stream Conditions

To model a general HIAD vehicle near peak radiative heating, a 70 degree sphere cone with a nose radius of 3.75 m, shoulder radius of 0.375 m, and a maximum diameter of 15 m is considered throughout this work. Increasing or decreasing the size of the vehicle by a factor of two will not significantly change the conclusions of this study. This is because, for Mars entry, the majority of the radiative heating is emitted from the nonequilibrium region of the shock layer, which is essentially unchanged by the size of the vehicle for a given free-stream condition. This trend is not consistent with lunar-return Earth entry vehicles, where the radiative heating (which is equilibrium dominated) increases nearly linearly with the vehicle size.

The majority of this paper will focus on three free-stream conditions, all with a free-stream velocity of 7 km/s. The first two conditions, which have free-stream densities (ρ_{inf}) of 5e-5 kg/m^3 (0.011 Torr) and 1e-4 kg/m^3 (0.022 Torr), were chosen to capture thermochemical nonequilibrium effects. As will be shown, the entire shock layer is in chemical nonequilibrium for these cases. The third condition has a free-stream density of 5e-4 kg/m^3 (0.110 Torr), which is chosen to produce a flowfield that includes both nonequilibrium and equilibrium regions, as well as increased radiative flux magnitudes. For all cases the angle of attack is set to zero and the free-stream temperature is set to 150 K. The free-stream composition for all cases is assumed to be 96% CO_2 and 4% N_2, by mole, to be consistent with recent EAST measurements.

The angle of attack is set to zero for all cases to simplify the flowfield modeling to axisymmetric grids. For this study, a shock adapted grid with 128 cells in the normal direction and 48 cells along the body is applied. Grid clustering around the shock is required for accurate radiative heating predictions because of the significant emission from the nonequilibrium shock region.

The influence of thermochemical nonequilibrium on the present flight conditions is shown in Figs. 1 – 3, which compare the stagnation line temperature and radiative flux profiles for two-temperature thermochemical nonequilibrium and single-temperature chemical equilibrium simulations. For the 5e-5 kg/m^3 and 1e-4 kg/m^3 cases, Figs. 1(a) and 2(a) show that the entire shock layer is in chemical nonequilibrium, while thermodynamic nonequilibrium is relatively small (as indicated by the rapid equilibration of the two temperatures behind the shock). Consequently, Figs. 1(b) and 2(b) show a significant difference between the equilibrium and nonequilibrium wall-directed radiative flux. The majority of the emission for the nonequilibrium case is located directly behind the shock, while for the equilibrium case the emission is nearly constant throughout the shock layer. Similar trends are seen in Fig. 3 for the higher density 5e-4 kg/m^3 case, although the differences in temperature and radiative flux are smaller between the equilibrium and nonequilibrium cases.

The radiative flux spectrum at the wall is presented in Fig. 4 for the ρ_{inf} = 1e-4 kg/m^3 case. This figure includes only the molecular band contribution for clarity (the atomic line contribution is less than 3% of the total radiative flux). The significant contribution from the CO 4th Positive band in the wavelength region between 120 and 220 nm is seen. Emission from the CO 4th Positive band originates mostly in the nonequilibrium region of the shock layer. This is shown in Fig. 5, which presents the volumetric radiance along the stagnation line resulting individually from the CO 4th Positive and CN Violet bands. The radiative flux profile is also shown in this figure. The sharp increase in the radiative flux due to the spike in CO 4th Positive emission is shown in this figure. Modeling this spike is therefore important for accurately modeling the radiative flux. The EAST measurements considered in the next section provide a means for validating our prediction capability of this nonequilibrium emission spike. The radiative flux contributions from other band systems are presented individually in Figs. 6 and 7. The CN Violet band is seen to be the second largest contributor to the radiative flux. The CN Violet emission originates mostly in the equilibrium region
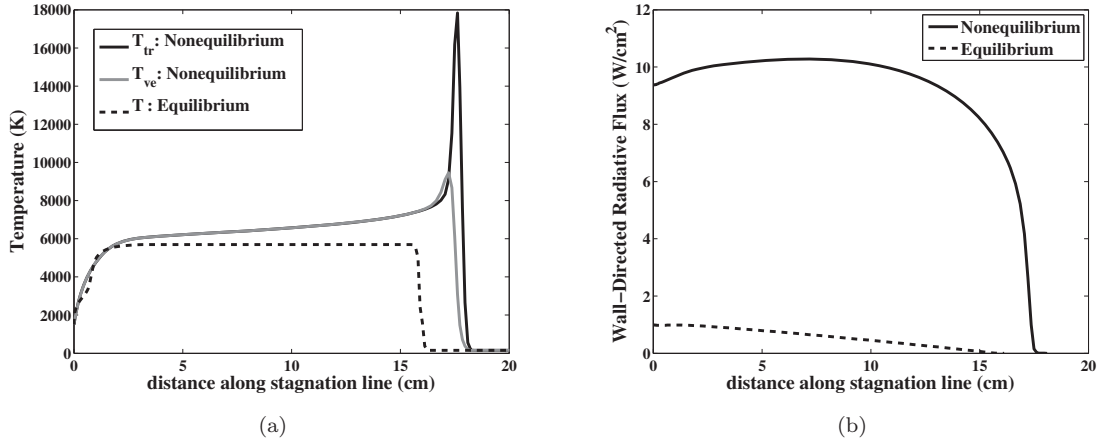
Figure 1: Stagnation line temperature and radiative flux profiles for the $\rho_{inf} = $ 5e-5 kg/m^3 (0.011 Torr) case.
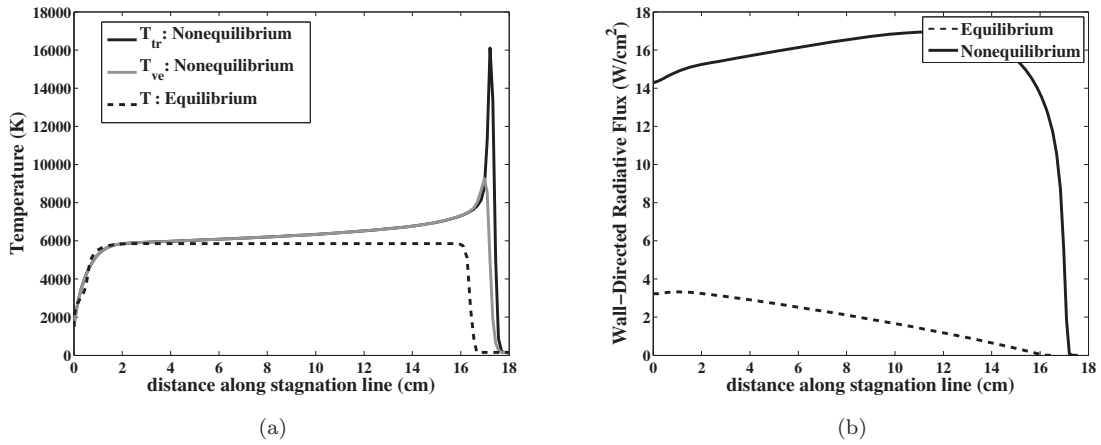

Figure 2: Stagnation line temperature and radiative flux profiles for the $\rho_{inf} = $ 1e-4 kg/m^3 (0.022 Torr) case.
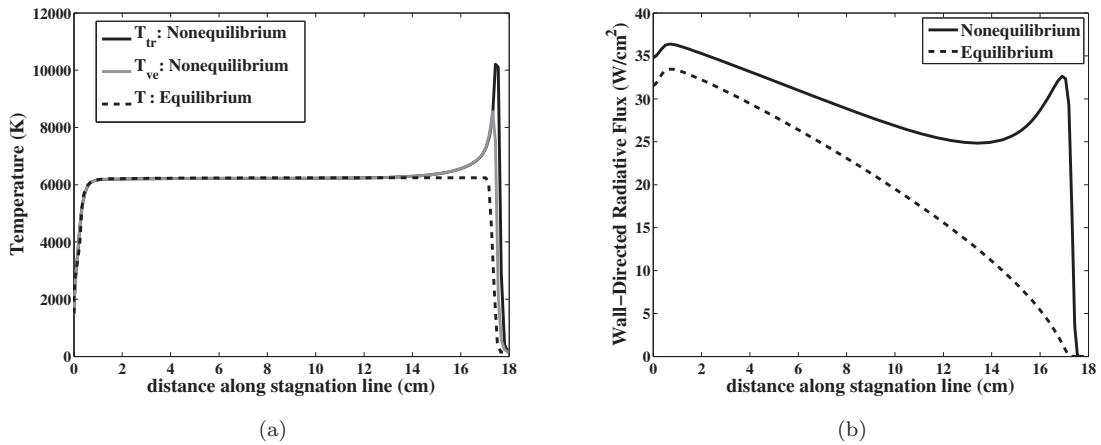

Figure 3: Stagnation line temperature and radiative flux profiles for the $\rho_{inf} = $ 5e-4 kg/m^3 (0.110 Torr) case.

of the shock layer. The contributions from the equilibrium and nonequilibrium region of the shock layer are studied in more detail in Appendix A, which simplifies the shock layer into two constant property layers: one layer representing the strongly emitting nonequilibrium region behind the shock and one layer representing the strongly absorbing region containing the rest of shock layer. This simplified model, which allows the radiative transport equations to be solved analytically, provides insight into the emission and absorption from these two distinct shock layer regions.
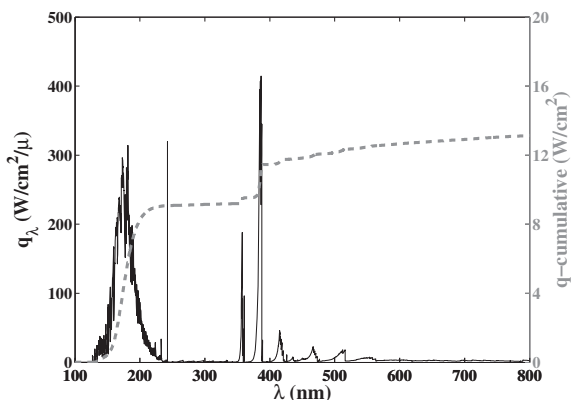
Figure 4: Total radiative flux spectrum for the $\rho_{inf} = $ 1e-4 kg/m^3 case (atomic radiation removed for clarity).
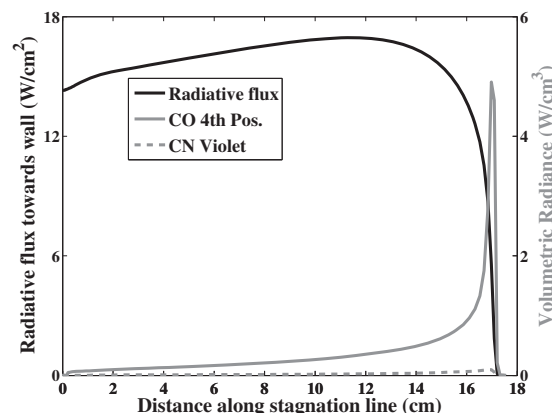
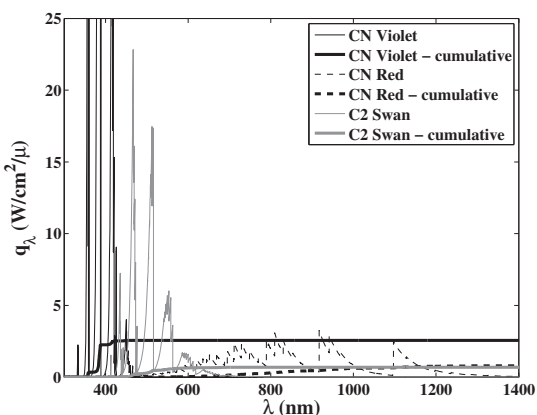Figure 5: Volumetric radiance and radiative flux along the stagnation line for the $\rho_{inf} = $ 1e-4 kg/m^3 case.

Figure 6: Radiative flux from individual band systems of CN and C$_2$ for the $\rho_{inf} = $ 1e-4 kg/m^3 case.

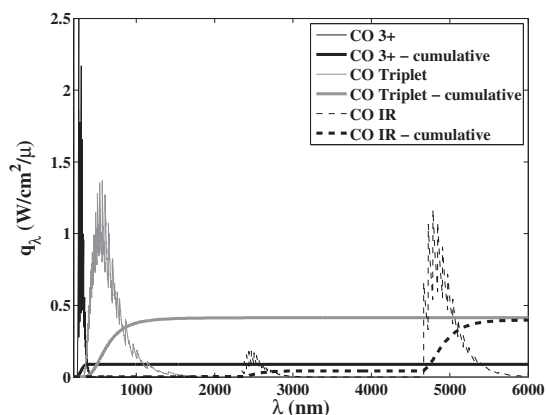Figure 7: Radiative flux from individual band systems of CO for the $\rho_{inf} = $ 1e-4 kg/m^3 case.

IV. Modifications to the Heritage Chemical Kinetics Model

Because of the significant contribution from nonequilibrium radiation to the total radiative heating for Mars entry, the most important flowfield modeling parameters are the chemical kinetic rates. The present section presents the chemical kinetic rate model used throughout this work.

A. Baseline Rate Model

The chemical kinetic rate model presented by Park et al.[4] has been applied in the majority of previous Mars entry radiation studies, and will therefore be referred to here as the "heritage" model. For this model, the important CO and CO$_2$ dissociation rates were chosen by Park et al.[4] based on comparisons with limited measurements by Davies[22] and Nealy,[23] respectively. Park et al.[4] applied a one-dimensional shock-fitting flowfield model for simulating the measurements and tuning the rates. As shown in Fig. 8, applying the heritage rates (along with Park et al.'s[4] vibrational relaxation parameters) using the present shock capturing LAURA flowfield model results in a factor of three over-prediction of the measurements of Nealy[23] (the uncalibrated Nealy data was scaled to agree in the equilibrium region). This discrepancy

suggests the heritage rate model should be reassessed using the same modern shock-capturing Navier-Stokes codes used for actual vehicle shock layer radiation predictions. This reassessment will be presented in the next subsection using recently published EAST and X2 shock tube measurements. The resulting rate model, which will be shown to compare well with experiments across a wide range of pressures and velocities, is presented in Tables 1 and 2. The rates listed in these tables will be referred to throughout this paper as the "baseline" model. This name is chosen because these rates represent the baseline from which kinetic rate uncertainties are assessed in the next section. From the coefficients listed in Tables 1 and 2, the forward rate constant is obtained for reaction i as follows:

$$k_{f,i} = A_{f,i} T_{f,i}^{n_{f,i}} exp(-D_{f,i}/T_{f,i}) \tag{1}$$

The last column in these tables presents the factor F_i, which represents the baseline rate divided by the heritage rate,[4] with both at a temperature of 8000 K. A "N/A" is listed for rates that are not included in the heritage model. An F_i value of unity indicates that the baseline rate is identical to that in the heritage model.
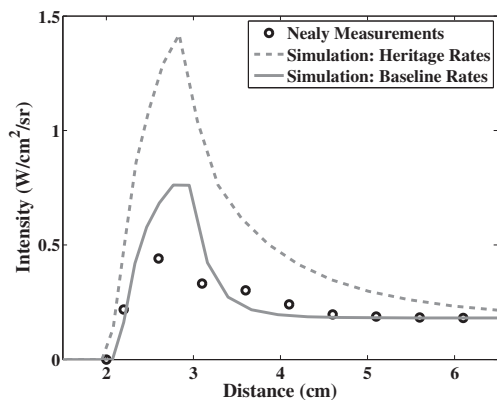

Figure 8: Radiative intensity for the Nealy experiment[23] considered by Park et al.[4] at 0.3 Torr and 9.05 km/s.
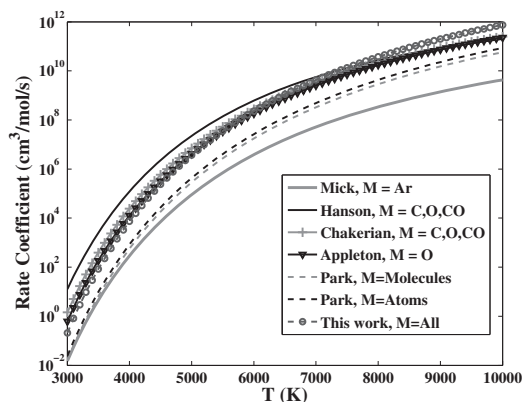

Figure 9: Comparison of CO dissociation rates.

The average temperature for dissociation, T_a, listed in Tables 1 and 2 as the rate controlling temperature for dissociation reactions, is assumed equal to $(T_{ve} T_{tr})^{1/2}$, as suggested by Park et al.[4] Uncertainties due to this modeling of T_a are assumed to be captured in the rate uncertainties chosen in Section V. While tuning the rates to fit the 0.25 Torr EAST data (as discussed in the next subsection), the modeling of T_a has a negligible influence because the two temperatures equilibrate almost immediately behind the shock. Note that for the flight cases presented in Figs. 1–3, this rapid equilibration is seen even though the free-stream pressures are well below 0.25 Torr.

The reference sources for the various chosen rates are listed in Tables 1 and 2. The rates labelled "This work" were chosen to provide the best fit with EAST data. The remainder of the rates, which have a smaller influence on the shock tube radiation, were obtained from recent aerothermodynamic studies or set equal to the heritage value. The rates chosen in this work to fit the EAST data are generally within the scatter of proposed rates from past researchers. For example, the largest deviation from the heritage model (among the "This work" rates) is present for the CO dissociation reaction, which is chosen to be 13 times larger than the heritage rate. As shown in Fig. 9, this significant increase in the CO dissociation rate is at the upper limit of previously proposed values.

B.   Comparisons with Experimental Data

In the present comparisons with EAST measurements, the baseline flowfield and radiation models defined in the previous section are applied, except for the chemical kinetic model, which will be specified as either the baseline or heritage model. Flowfield-radiation coupling is accounted for in all simulations. This tends to slightly decrease the peak vibrational-electronic temperature behind the shock, and therefore decrease the level of peak radiative emission. To simulate the spatial smearing of the measurements, the simulated radiation profiles are averaged at each spatial point over 0.5 and 0.3 cm for the 165–215 nm and 340–440 nm spectral ranges, respectively.

American Institute of Aeronautics and Astronautics

Table 1: Chemical kinetics for neutral species applied in the present baseline model.

i	Reaction	$A_{f,i}$	$n_{f,i}$	$D_{f,i}$	$T_{f,i}$	Third Body, M	Ref.	F_i
1	$CO_2 + M \leftrightarrow CO + O + M$	2.8e+22	-1.50	6.328e+4	T_a	N, C, O	This work	2
		1.4e+22	-1.50	6.328e+4	T_a	others	This work	2
2	$CO + M \leftrightarrow C + O + M$	3.0e+21	-1.00	1.29e+5	T_a	All	This work	13
3	$C_2 + M \leftrightarrow 2C + M$	4.5e+18	-1.00	7.15e+4	T_a	All	This work	1.25
4	$CN + M \leftrightarrow C + N + M$	6.0e+15	-0.4	7.10e+4	T_a	All	Fujita et al.[24]	0.66
5	$N_2 + M \leftrightarrow 2N + M$	3.0e+22	-1.60	1.132e+5	T_a	N, C, O	Park[25]	1
		6.0e+3	2.6	1.132e+5	T_{ve}	e^-	Bourdon et al.[26]	1.2e-5
		7.0e+21	-1.60	1.132e+5	T_a	others	Park[25]	1
6	$NO + M \leftrightarrow N + O + M$	1.1e+17	0.00	7.55e+4	T_a	N, C, O, NO, CO_2	Park[25]	1
		5.0e+15	0.00	7.55e+4	T_a	others	Park[25]	1
7	$O2 + M \leftrightarrow 2O + M$	1.0e+22	-1.50	5.936e+04	T_a	N, C, O	Park[25]	1
		2.0e+21	-1.50	5.936e+04	T_a	others	Park[25]	1
8	$CO_2 + O \leftrightarrow O_2 + CO$	2.71e+14	0.0	3.38e+4	T_{tr}		Ibragimova[27]	6
9	$CO + C \leftrightarrow C_2 + O$	2.4e+17	-1.00	5.80e+4	T_{tr}		Park et al.[4]	1
10	$CO + N \leftrightarrow CN + O$	1.0e+14	0.00	3.86e+4	T_{tr}		Park et al.[4]	1
11	$CO + NO \leftrightarrow CO_2 + N$	3.0e+6	0.88	1.33e+4	T_{tr}		Fujita et al.[24]	N/A
12	$CO + O \leftrightarrow O_2 + C$	3.9e+13	-0.18	6.92e+4	T_{tr}		Park et al.[4]	1
13	$C_2 + N_2 \leftrightarrow CN + CN$	1.5e+13	0.0	2.1e+4	T_{tr}		Gokcen[28]	N/A
14	$CN + C \leftrightarrow C_2 + N$	3.0e+14	0.00	1.81e+4	T_{tr}		Fujita et al.[24]	3.2
15	$CN + O \leftrightarrow NO + C$	1.6e+12	0.10	1.46e+4	T_{tr}		This work	0.1
16	$N + CO \leftrightarrow NO + C$	1.1e+14	0.07	5.35e+4	T_{tr}		Fujita et al.[24]	N/A
17	$N_2 + C \leftrightarrow CN + N$	1.1e+14	-0.11	2.32e+4	T_{tr}		Park et al.[4]	1
18	$N_2 + CO \leftrightarrow CN + NO$	1.2e+16	-1.23	7.70e+4	T_{tr}		Fujita et al.[24]	N/A
19	$N_2 + O \leftrightarrow NO + N$	6.0e+13	0.1	3.80e+4	T_{tr}		Fujita et al.[24]	1.9
20	$O_2 + N \leftrightarrow NO + O$	2.49e+9	1.18	4.01e+3	T_{tr}		Bose & Candler[29]	2.2

Table 2: Chemical kinetics for ionized species applied in the present baseline model.

i	Reaction	$A_{f,i}$	$n_{f,i}$	$D_{f,i}$	$T_{f,i}$	Ref.	F_i
21	$C + O \leftrightarrow CO^+ + e^-$	8.8e+8	1.0	3.31e+4	T_{tr}	Park et al.[4]	1
22	$C + e^- \leftrightarrow C^+ + 2e^-$	3.7e+31	-3.0	1.307e+5	T_{ve}	Park et al.[30]	10.5
23	$C^+ + CO \leftrightarrow CO^+ + C$	1.0e+13	0.0	3.14e+4	T_{tr}	Park et al.[4]	1
24	$CO + e^- \leftrightarrow CO^+ + 2e^-$	4.5e+14	0.275	1.63e+5	T_{ve}	Teulet et al.[31]	N/A
25	$N + O \leftrightarrow NO^+ + e^-$	5.30e+12	0.0	3.19e+4	T_{tr}	Park et al.[32]	1
26	$NO^+ + C \leftrightarrow C^+ + NO$	1.0e+13	0.0	2.32e+4	T_{tr}	Park et al.[4]	1
27	$NO^+ + N \leftrightarrow O^+ + N_2$	3.40e+13	-1.08	1.28e+4	T_{tr}	Park[25]	1
28	$NO^+ + O \leftrightarrow O_2^+ + N$	7.20e+12	0.29	4.86e+4	T_{tr}	Park[25]	1
29	$NO^+ + O_2 \leftrightarrow NO + O_2^+$	2.40e+13	0.41	3.26e+4	T_{tr}	Park[25]	N/A
30	$O + O \leftrightarrow O_2^+ + e^-$	7.10e+02	2.7	8.06e+4	T_{tr}	Park[32]	1
31	$O + e^- \leftrightarrow O^+ + 2e^-$	3.90e+33	-3.78	1.585e+5	T_{ve}	Park[25]	1
32	$O_2 + C^+ \leftrightarrow O_2^+ + C$	1.00e+13	0.0	9.40e+3	T_{tr}	Park et al.[4]	1
33	$O_2^+ + O \leftrightarrow O^+ + O_2$	4.00e+12	-0.09	1.80e+4	T_{tr}	Park[32]	1
34	$O_2 + e^- \leftrightarrow O_2^+ + 2e^-$	2.19e+10	1.16	1.30e+5	T_{ve}	Teulet et al.[31]	N/A

American Institute of Aeronautics and Astronautics

EAST measurements are available[11] at pressures of 0.25, 0.10, and 0.05 Torr. Although the two lower pressures are more flight relevant, the 0.25 Torr cases are valuable for assessing the nonequilibrium chemistry because the non-Boltzmann influence is small, and therefore disagreements between measurements and simulations are attributed to inadequacies in the chemical rates and not the non-Boltzmann excitation rates. Similarly, the two temperatures are equilibrated almost immediately behind the shock, which reduces the sensitivity of the simulations to translational-vibrational relaxation parameters. For these reasons, the 0.25 Torr cases were used to tune the "This work" rates in Table 1. Comparisons with the 0.25 Torr cases are presented next, followed by comparisons with the more flight relevant 0.10 and 0.05 Torr cases.

Comparisons between the baseline or heritage rate simulations and the 0.25 Torr EAST measurements are presented in Figs. 10–12. In (a) and (b) of these figures, the spatial profile of J_c is presented, which is defined as the integrated intensity (over the two specified spectral ranges) divided by the shock tube diameter of 10.16 cm. The 165–215 nm range considered in (a) captures a significant fraction of the important CO 4th Positive band system, while the 340–440 nm range in (b) captures a majority of the CN Violet band system. Considering the 165–215 nm range, a factor of 3–4 over-prediction of the peak radiance is seen for the heritage rates, in addition to a significantly larger region of nonequilibrium. This significant over-prediction of the CO 4th Positive emission suggests that the simulated CO number density is too large. As discussed previously, a factor of 13 increase in the CO dissociation rate was chosen for the baseline model to correct this over-prediction. The factor of 2 increase in the CO_2 dissociation rate and the choice of the Ibragimova[27] rate for the reaction $CO_2 + O \leftrightarrow O_2 + CO$ also reduced the over-prediction by decreasing the CO_2 number density and therefore reducing the temperatures in the nonequilibrium region (the increase in CO number density from these changes is more than offset by the temperature decrease). The chosen baseline rates are seen to significantly improve the agreement with the measurements.

Considering the CN Violet emission in the 340–440 nm range, a less extreme over-prediction is seen for the heritage rates than was seen for the CO 4th Positive band. The rates chosen previously to improve the CO 4th Positive emission result in a significant decrease in the nonequilibrium temperatures, which cause a strong decrease in the CN Violet emission (through a reduction in the total CN number density). This decrease is slightly more than is required for agreement with measurements. A factor of 10 decrease in the rate for the reaction $CN + O \leftrightarrow NO + C$ was therefore chosen to offset this decrease. The resulting baseline rates are seen to provide improved predictions of the nonequilibrium CN Violet emission, although slight under-predictions of the peak emission remain. To improve the agreement further would require sacrificing the excellent agreement seen for the CO 4th Positive. The nonequilibrium emission from the CO 4th Positive band is significantly larger than the CN Violet band, so preference was given to achieving the best agreement for the CO 4th Positive band.

To further validate the rates chosen for the baseline rate model, the baseline rate simulation and measured spectrum at the peak nonequilibrium point and an equilibrium point are presented in (c)–(f) of Figs. 10–12. Except for Fig. 11(d), good agreement is seen between the simulated and measured spectra. These comparisons confirm that the good agreement seen in the spatial profiles of (a) and (b) are not due to a fortuitous cancellation of various spectral regions. In the nonequilibrium regions, (c) shows that the peak nonequilibrium emission of the CO 4th Positive band, which contributes significantly the radiative flux for a flight case, is simulated accurately with the baseline rate model. Similarly, good agreement is seen in (d) for the nonequilibrium emission of the CN Violet band, although it is not quite as good as that seen for the CO 4th Positive band. In the equilibrium region, (e) and (f) show excellent agreement for both band systems.

The good agreement between the baseline rate results and 0.25 Torr measurements was seen because the rates were chosen to force this agreement. Comparisons with experiments at other conditions, specifically flight relevant pressures of 0.1 and 0.05 Torr, will therefore define the quality of the baseline rate model. These comparisons are made in Figs. 13 and 14 for a pressure of 0.1 Torr and Figs. 15 and 16 for a pressure of 0.05 Torr. As with the 0.25 Torr cases, (a) and (b) present the integrated profile for the CO 4th Positive and CN Violet bands. The agreement between the baseline simulation and measured profiles are seen to be nearly as good as that seen previously for the 0.25 Torr cases. Note that unlike the 0.25 Torr cases, these lower pressure cases do not reach chemical equilibrium within the test time. The slight differences seen near the end of the test time may be a result of driver gas contamination in this region of the flow. Similarly to the 0.25 Torr results, the heritage rate is seen to significantly over-predict the CO 4th Positive band and, to a lesser extent, the CN Violet band.
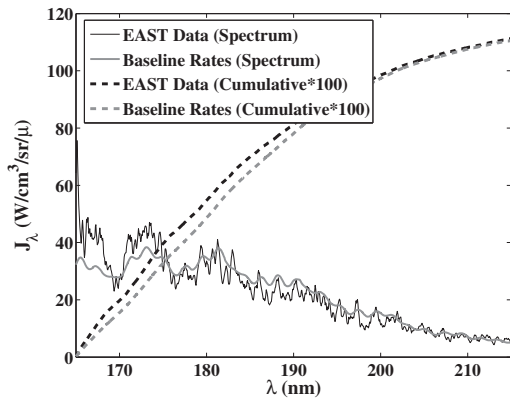
The spectral comparisons presented in (c)–(f) of Figs. 13–16 show surprisingly good agreement between the baseline simulations and measurements at two nonequilibrium spatial points (unlike the 0.25 Torr cases,
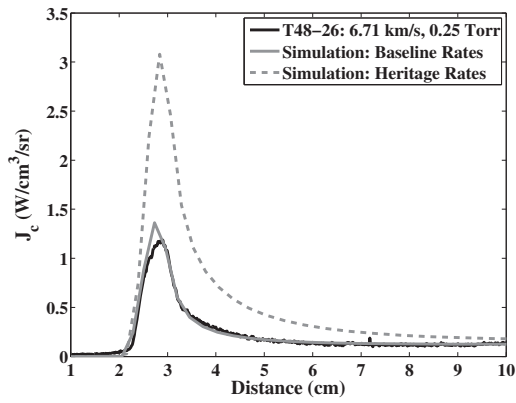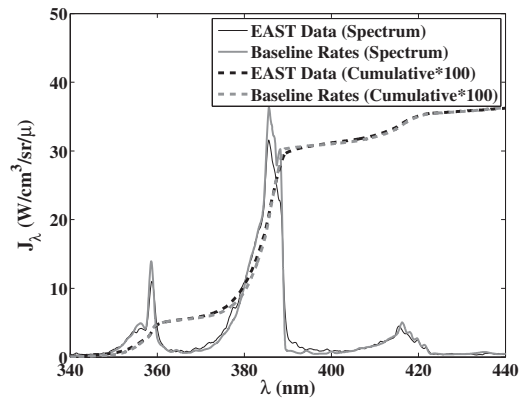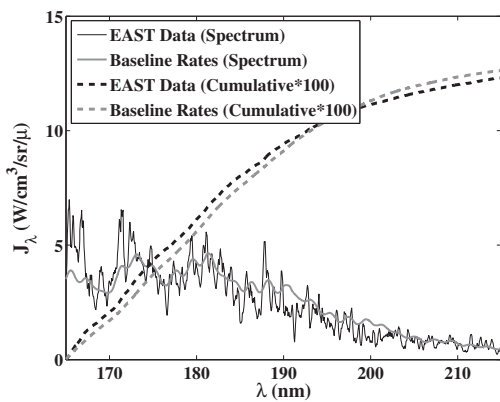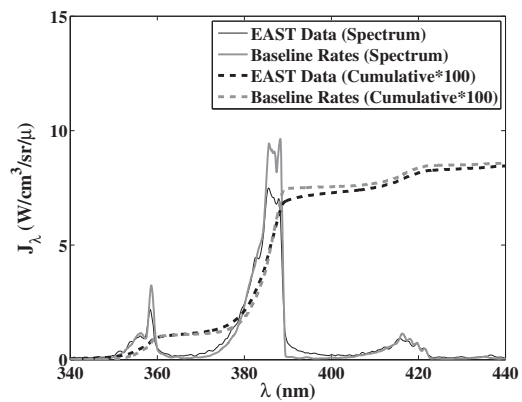
(a) 165–215 nm
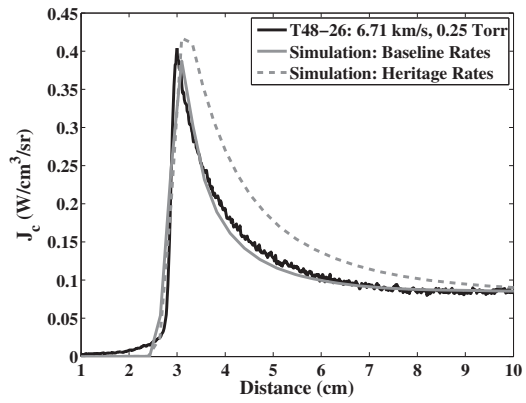
(b) 340-440 nm
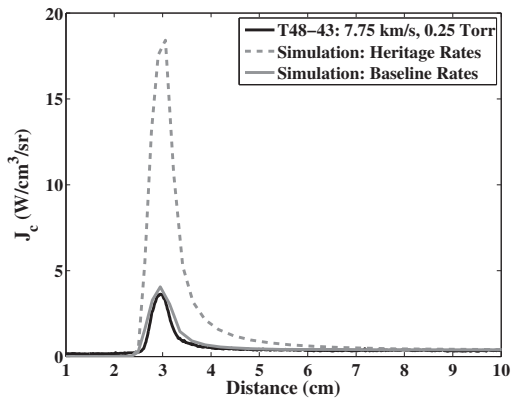
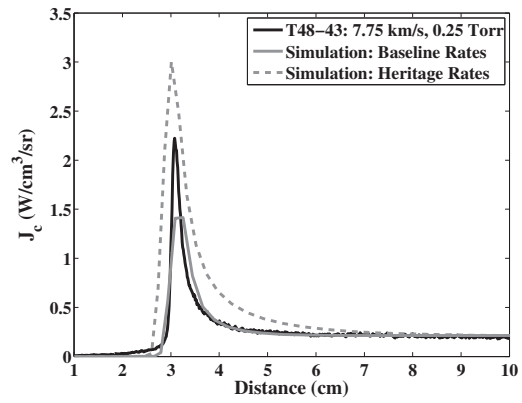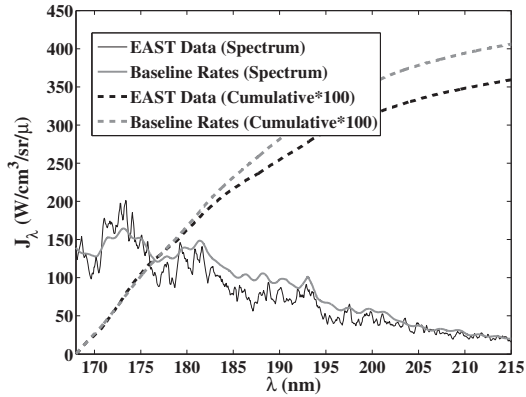(c) Distance = 3.0 cm

(d) Distance = 3.0 cm

(e) Distance = 9.0 cm

(f) Distance = 9.0 cm

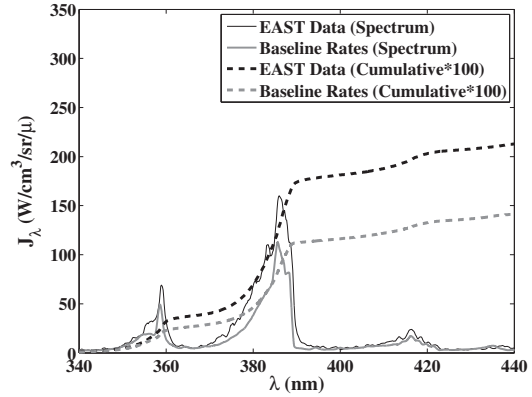Figure 10: Comparison of nonequilibrium profiles for Test 51, Shot 2 at 6.71 km/s and 0.25 Torr.

American Institute of Aeronautics and Astronautics

(a) 165–215 nm

(b) 340-440 nm

(c) Distance = 3.0 cm

(d) Distance = 3.0 cm

(e) Distance = 7.0 cm

(f) Distance = 7.0 cm

Figure 11: Comparison of nonequilibrium profiles for Test 48, Shot 43 at 7.75 km/s and 0.25 Torr.

American Institute of Aeronautics and Astronautics

(a) 165–215 nm

(b) 340-440 nm

(c) Distance = 3.0 cm

(d) Distance = 3.0 cm

(e) Distance = 8.0 cm

(f) Distance = 8.0 cm

Figure 12: Comparison of nonequilibrium profiles for Test 48, Shot 39 at 7.82 km/s and 0.25 Torr.
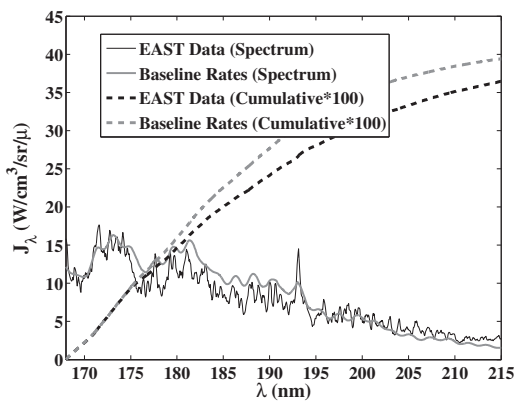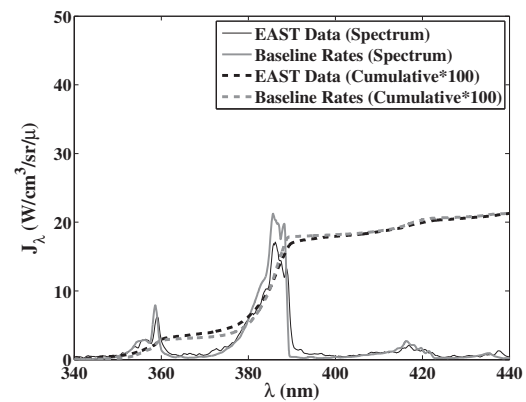
(a) 165–215 nm

(b) 340-440 nm

(c) Distance = 3.0 cm

(d) Distance = 3.0 cm

(e) Distance = 5.0 cm

(f) Distance = 5.0 cm

Figure 13: Comparison of nonequilibrium profiles for Test 51, Shot 40 at 6.72 km/s and 0.10 Torr.

American Institute of Aeronautics and Astronautics

(a) 165–215 nm

(b) 340-440 nm

(c) Distance = 2.8 cm

(d) Distance = 2.8 cm

(e) Distance = 5.0 cm

(f) Distance = 5.0 cm

Figure 14: Comparison of nonequilibrium profiles for Test 51, Shot 12 at 6.90 km/s and 0.10 Torr.

(a) 165–215 nm
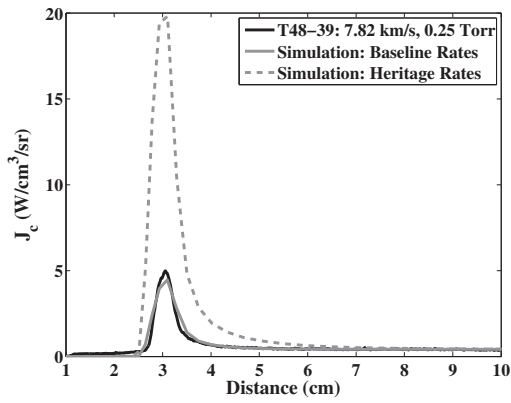
(b) 340-440 nm

(c) Distance = 3.2 cm

(d) Distance = 3.2 cm
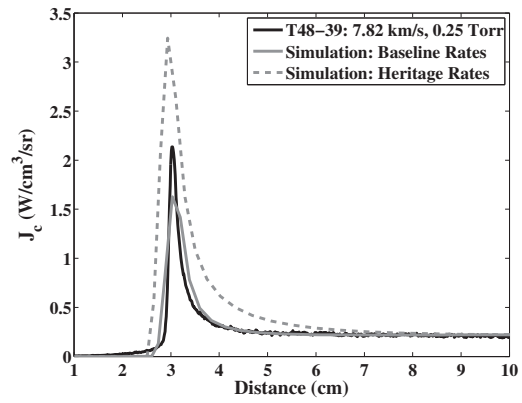
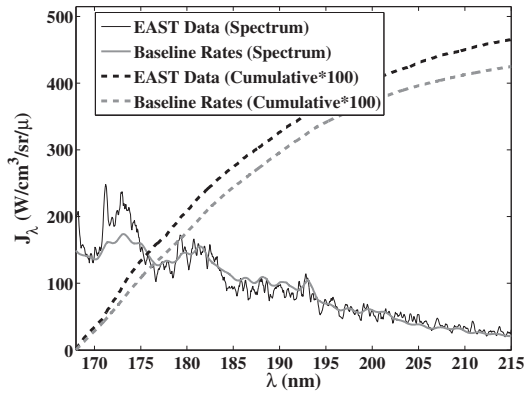(e) Distance = 4.5 cm

(f) Distance = 4.5 cm

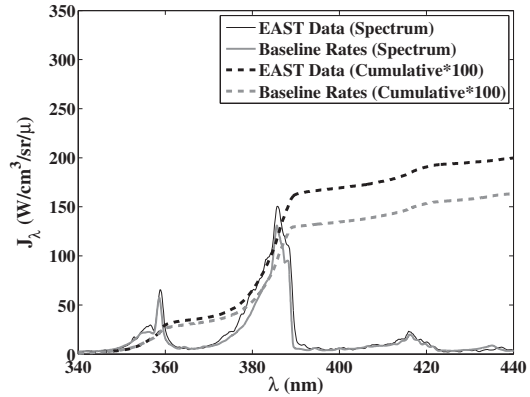Figure 15: Comparison of nonequilibrium profiles for Test 51, Shot 48 at 7.47 km/s and 0.05 Torr.
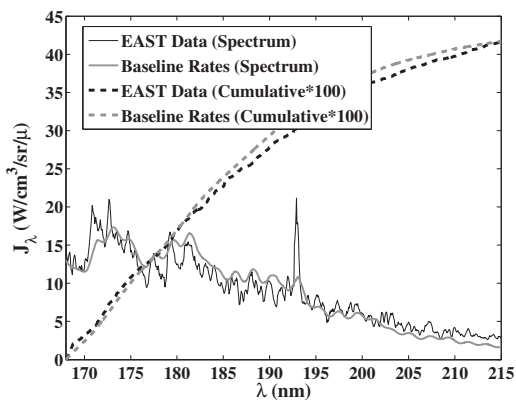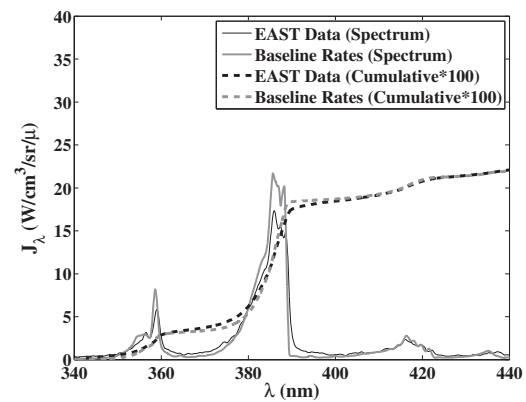
(a) 165–215 nm
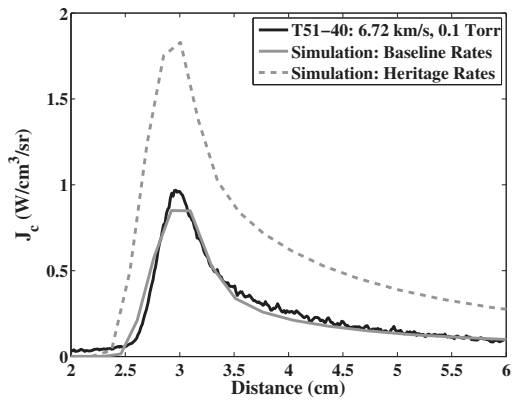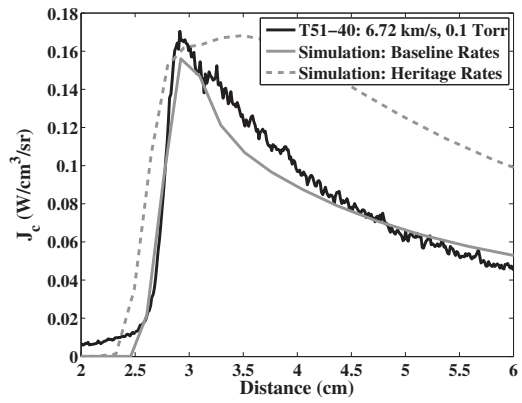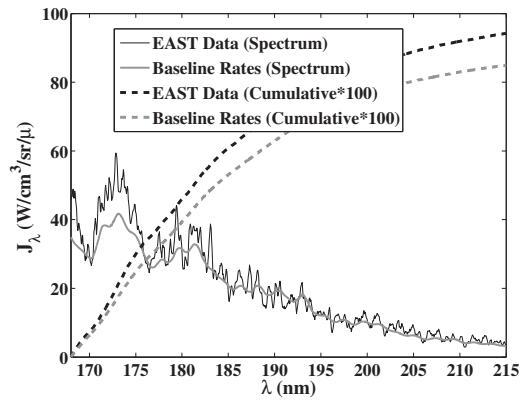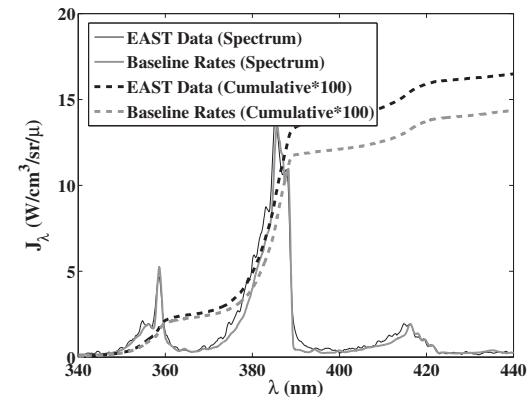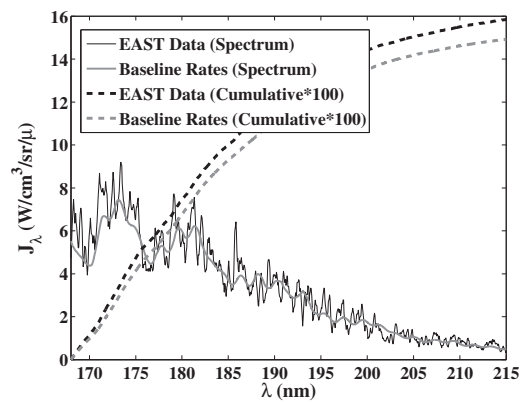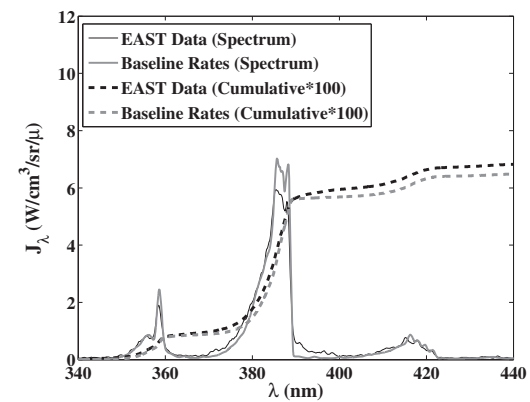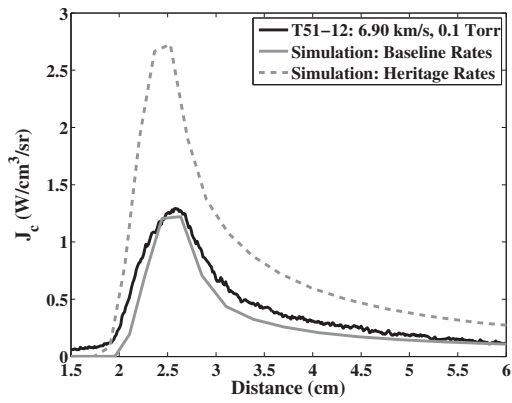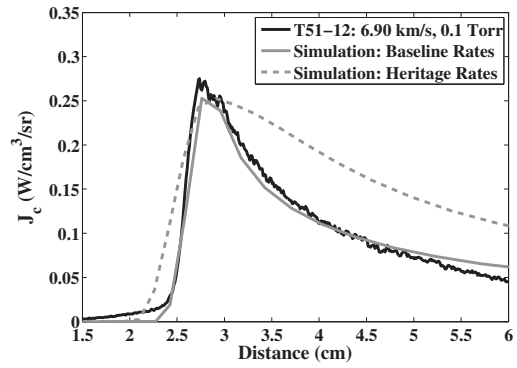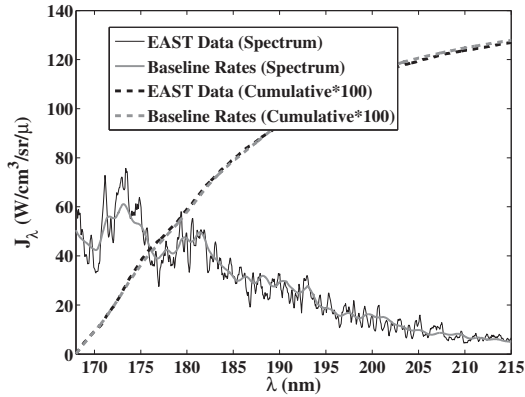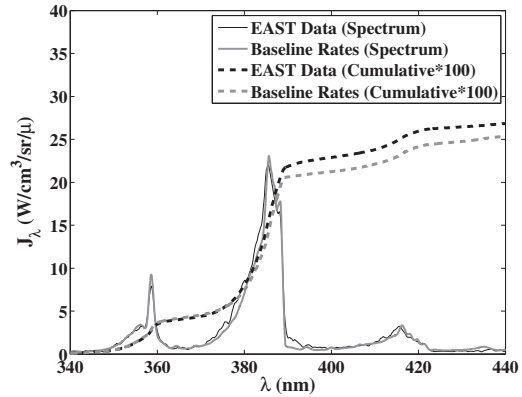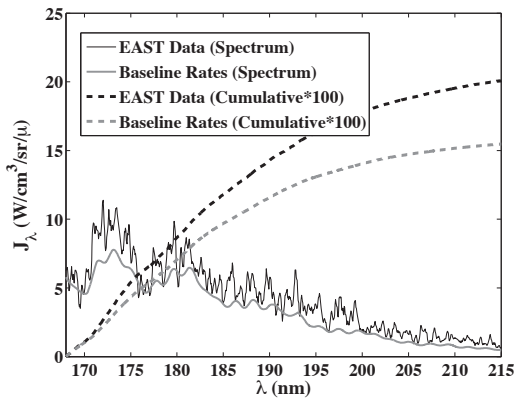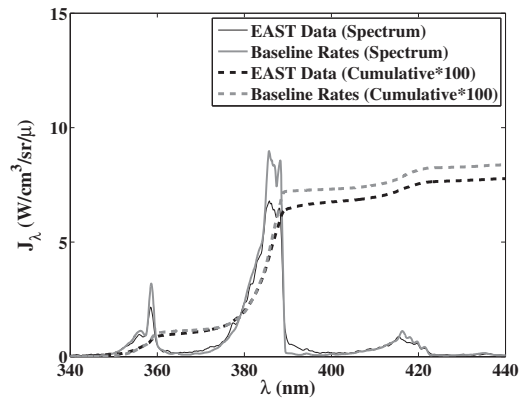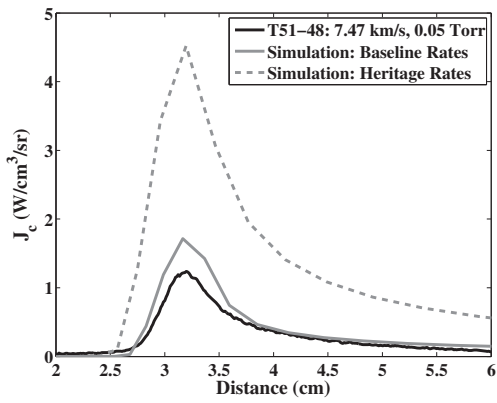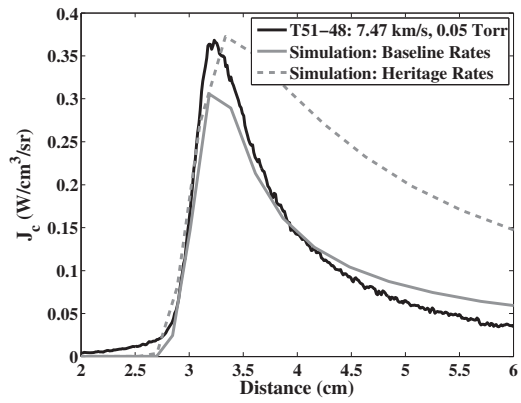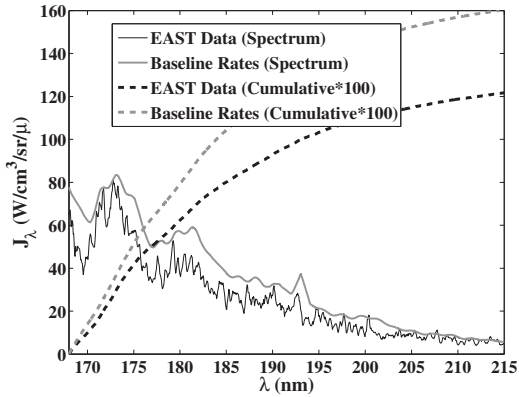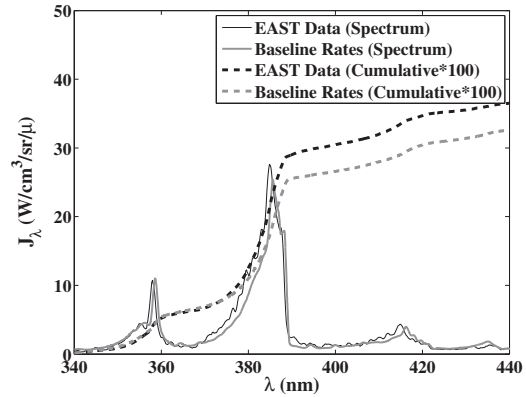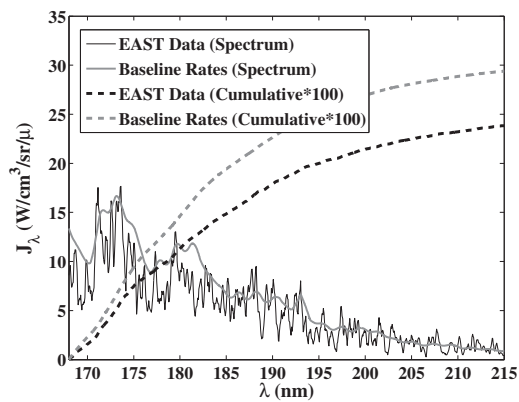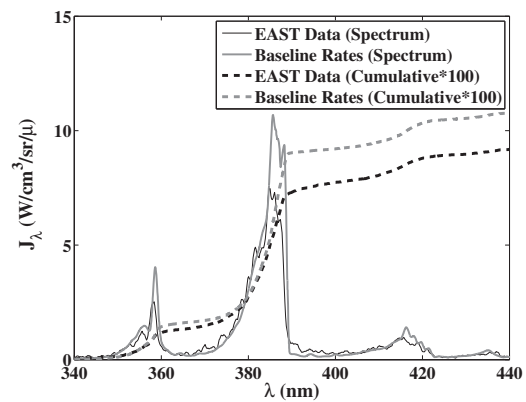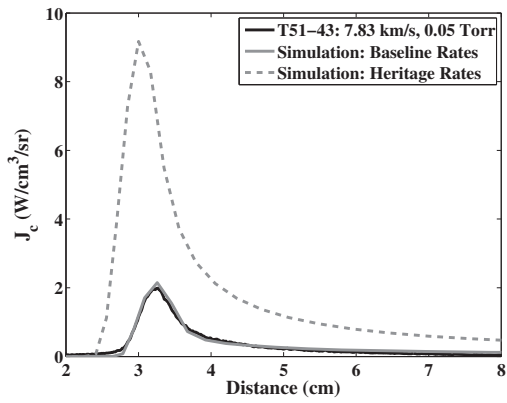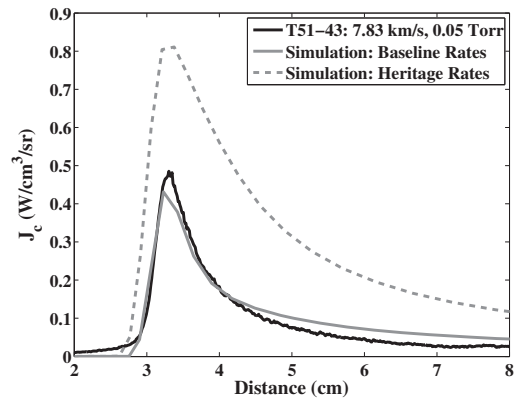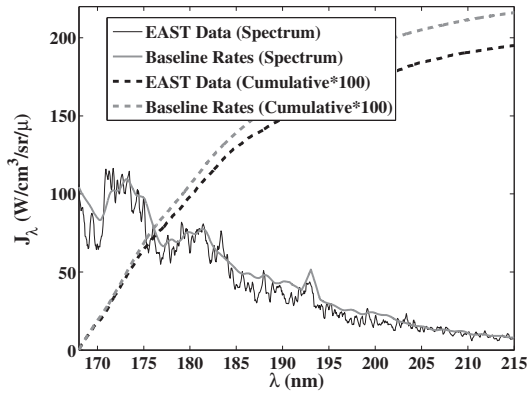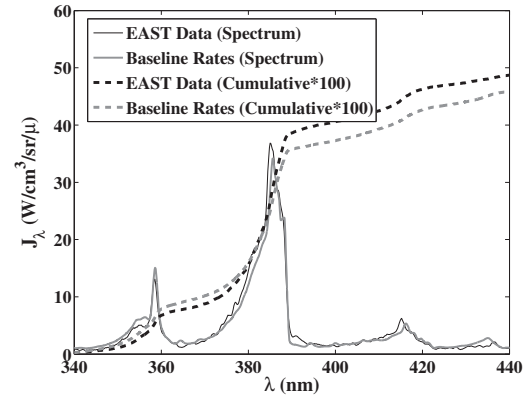
(b) 340-440 nm

(c) Distance = 3.3 cm

(d) Distance = 3.3 cm
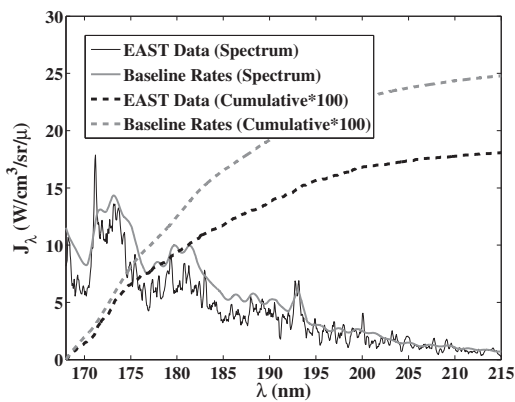
(e) Distance = 5.3 cm
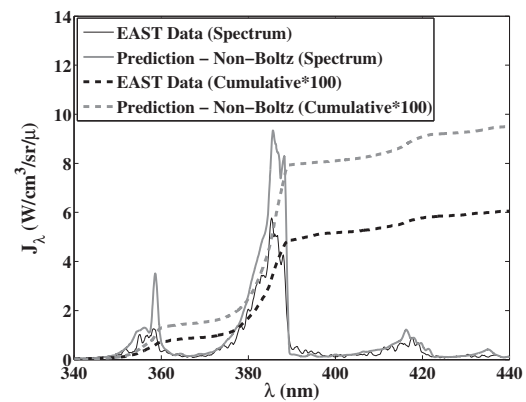
(f) Distance = 5.3 cm

Figure 16: Comparison of nonequilibrium profiles for Test 51, Shot 43 at 783 km/s and 0.05 Torr.

American Institute of Aeronautics and Astronautics

both spatial points are in nonequilibrium because equilibrium is not reached during the test time). Especially good agreement at the point of peak emission is seen in (c) and (d) of these figures. The poorer agreement for the downstream point in (e) and (f) suggests further that driver gas contamination may be influencing this region of the flow. Recall that the 0.25 Torr cases confirm that the approach to equilibrium is properly simulated with the baseline rate model.

To test the quality of the chosen baseline rates further, a measurement of the CN Violet at 0.1 Torr made in the X2 facility[33] is considered. The measured integrated radiance between 310–450 nm is presented in Fig 17 and compared with the results of the baseline and heritage rate models. The baseline rate model is seen to provide excellent agreement with the measurements, which provides further confidence in the chosen rates. The heritage rate model is seen to significantly over-predict the measurements. This is consistent with the over-prediction reported by Palmer et al.[34] using the heritage rate model.

Figure 17: Comparison of nonequilibrium profiles for X2 measurements at 8.6 km/s and 0.1 Torr.

V.   Uncertainty Contribution due to Flowfield Modeling Parameters

This section examines the sensitivity of the radiative flux to flowfield modeling parameters and determines the radiative flux uncertainty due to these parameters. The HIAD flight cases considered in previous sections are the focus of this analysis. The radiative flux sensitivities to chemical kinetic rates are presented in subsection A, while the sensitivities to vibrational relaxation parameters are presented in subsection B. Finally, the radiative flux uncertainty due to these parameters is assessed in subsection C.

A.   Radiative Flux Sensitivities to Chemical Kinetic Rates

The sensitivity of the radiative flux to each chemical kinetic rate is found by changing the individual rate and recomputing the flowfield and radiation. This process is performed for a one order-of-magnitude increase and decrease in each rate listed in Table 1 (sensitivities for rates listed in Table 2 were found to all be less than 1% and are therefore not included in this table). The resulting percent change in the stagnation point radiative flux is presented in Table 3 for the 5e-5, 1e-4 and 5e-4 kg/m^3 HIAD cases at 7 km/s. The "$+\Delta k_f$" column represents the percent change in the radiative flux due to a one order-of-magnitude increase in each rate, while the "$-\Delta k_f$" column represents the percent change due to a one order-of-magnitude rate decrease. Sensitivities less than 1% are replaced by "–" in this table for clarity. Table 3 shows that the 5e-5 and 1e-4 kg/m^3 cases are more sensitive to the kinetic rates than the 5e-4 kg/m^3 case, which is expected because the former cases contain larger regions of thermochemical nonequilibrium. For all three cases the sensitivities to the dissociation rates for CO, NO, O_2, and CO_2 are seen to be significant. The one order-of-magnitude increase in the CO dissociation rate results in a 71.1%, 63.6%, and 17.0% decrease in the radiative flux for the 5e-5, 1e-4, and 5e-4 kg/m^3 cases, respectively. This radiative flux decrease is a result of lower CO number densities and temperatures, which decreases the emission of the strongly radiating CO 4th Positive system. This is shown in Fig. 18, which presents the sensitivity of the stagnation line temperature and radiative flux profiles to CO dissociation rate. It is seen that increasing the rate by one order-of-magnitude ($+\Delta k_{f,5}$) results in thermochemical equilibrium (identified by the constant temperature region) throughout a large fraction of the shock layer.

The reactions identified in Table 3 that provide the largest radiative heating sensitivity are studied in more detail in Table 4. This table lists references to studies that provide alternative rate values to those applied in the baseline model. Also listed are uncertainty bounds for each rate, which are assessed from the variation of these other proposed rates from the baseline rate. The abbreviation "om" stands for order-of-magnitude. Most of the uncertainties are seen to be directional, meaning the rates proposed by other researchers were either all above or all below the baseline value. The listed uncertainties are only approximate because the differences between the rates change with temperature (the listed uncertainties are evaluated at 7000 K). An example of the scatter in proposed rate values was shown previously in Fig. 9, which compares various rates for CO dissociation.
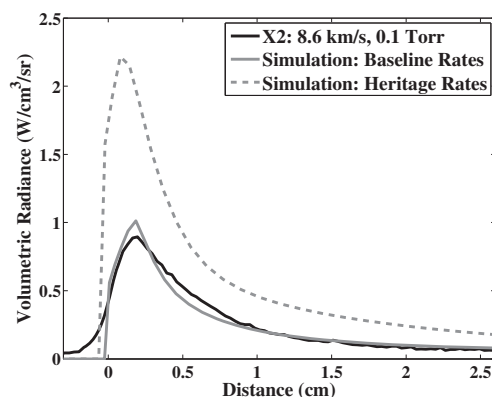
American Institute of Aeronautics and Astronautics

Table 3: Percent change in the stagnation-point radiative flux due to 1 order-of-magnitude changes in each reaction rate.

i	Reaction	$\rho_{inf} = 5 \times 10^{-5}$ kg/m³		$\rho_{inf} = 1 \times 10^{-4}$ kg/m³		$\rho_{inf} = 5 \times 10^{-4}$ kg/m³	
		$+\Delta k_f$	$-\Delta k_f$	$+\Delta k_f$	$-\Delta k_f$	$+\Delta k_f$	$-\Delta k_f$
1	$CO_2 + M \leftrightarrow CO + O + M$	4.6	-12.5	3.9	-11.6	–	–
2	$CO + M \leftrightarrow C + O + M$	-71.1	106.6	-63.6	102.8	-17.0	37.0
3	$C_2 + M \leftrightarrow 2C + M$	–	–	–	–	–	–
4	$CN + M \leftrightarrow C + N + M$	–	–	–	–	–	–
5	$N_2 + M \leftrightarrow 2N + M$	–	–	–	–	–	–
6	$NO + M \leftrightarrow N + O + M$	-10.5	10.0	-12.3	11.0	-2.70	3.51
7	$O2 + M \leftrightarrow O + O + M$	–	8.4	-1.3	6.9	–	2.36
8	$CO_2 + O \leftrightarrow O_2 + CO$	–	–	–	–	–	–
9	$CO + C \leftrightarrow C_2 + O$	–	–	–	–	–	–
10	$CO + N \leftrightarrow CN + O$	–	–	–	–	–	–
11	$CO + NO \leftrightarrow CO_2 + N$	–	–	–	–	–	–
12	$CO + O \leftrightarrow O_2 + C$	-2.1	–	-2.6	–	–	–
13	$C_2 + N_2 \leftrightarrow CN + CN$	–	–	–	–	–	–
14	$CN + C \leftrightarrow C_2 + N$	–	–	–	–	–	–
15	$CN + O \leftrightarrow NO + C$	-2.3	–	-2.6	–	-1.33	–
16	$N + CO \leftrightarrow NO + C$	-4.9	3.2	-5.3	4.2	-2.16	1.72
17	$N_2 + C \leftrightarrow CN + N$	7.0	-1.7	5.6	-1.4	2.30	–
18	$N_2 + CO \leftrightarrow CN + NO$	–	–	–	–	–	–
19	$N_2 + O \leftrightarrow NO + N$	–	7.4	–	6.7	–	–
20	$O_2 + N \leftrightarrow NO + O$	-1.1	1.0	-1.4	1.3	–	–

(a)

(b)
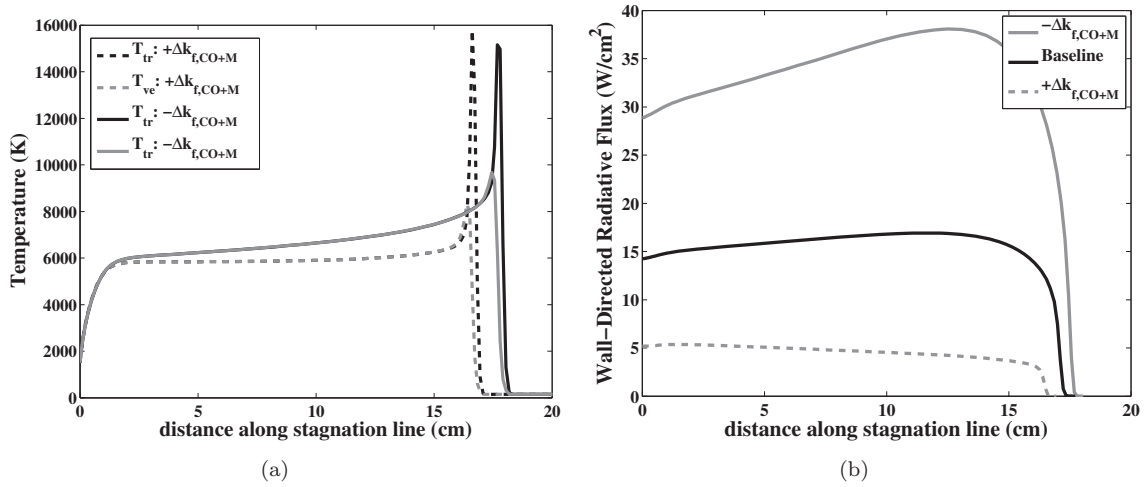
Figure 18: Dependence of stagnation line temperature and radiative flux profiles on the CO dissociation rate for the ρ_{inf} = 1e-4 kg/m³ case.

Table 4: Uncertainty values for most significant rates for radiative heating predictions.

#	Reaction	Data Sources	Uncertainty
1	$CO_2 + M \leftrightarrow CO + O + M$	[35–37]	+0, -1 om
2	$CO + M \leftrightarrow C + O + M$	[38–41]	+50, -75%
6	$NO + M \leftrightarrow N + O + M$	[42, 43]	+1, -1 om
7	$O_2 + M \leftrightarrow O + O + M$	[25]	+50, -50%
12	$CO + O \leftrightarrow O_2 + C$	[44, 45]	+1, -0 om
15	$CN + O \leftrightarrow NO + C$	[46, 47]	+1, -0 om
17	$N_2 + C \leftrightarrow CN + N$	[28]	+50, -50%
19	$N_2 + O \leftrightarrow NO + N$	[24, 30, 48]	+50, -50%

American Institute of Aeronautics and Astronautics

B. Vibrational Energy Relaxation Models

The two-temperature energy equation formulation presented by Lee[49] and Gnoffo et al.[50] is the basis for the Mars specific modeling parameters presented by Park et al.,[4] which are applied in the present baseline model. This formulation contains four terms that account for energy exchange between the translational-rotational and vibrational-electronic energy modes: 1) vibrational energy reactive source term, 2) electronic energy reactive source term, 3) vibrational-translational energy relaxation, and 4) electronic-translational energy relaxation. Of these four terms, only the vibrational-translational energy relaxation term is significant for the Mars entry cases of present interest. The modeling of this term and its influence on the radiative flux is the focus of this subsection.

The vibrational-translational energy relaxation term is written by Gnoffo et al.[50] as follows

$$Q_{v-t} = \rho C_{v,v} \frac{\sum_{i=mol.} X_i/\tau_{v,i}}{\sum_{i=mol.} X_i} \tag{2}$$

where $C_{v,v}$ is the vibrational-electronic specific heat, X_i is the mole fraction, and $\tau_{v,i}$ is the vibrational-translational relaxation time. The primary uncertainty in computing Q_{v-t} is the modeling of $\tau_{v,i}$, which itself is modeled with two components:

$$\tau_{v,i} = \tau_{v,i}^{MW} + \tau_{v,i}^{P} \tag{3}$$

where $\tau_{v,i}^{MW}$ is the Millikan and White component and $\tau_{v,i}^{P}$ is the Park high temperature correction. The $\tau_{v,i}^{MW}$ component is computed as follows:

$$\tau_{v,i}^{MW} = \frac{1}{p} \sum_j X_j \times exp\left[a_{LT,i,j}(T_{tr}^{-1/3} - b_{LT,i,j}) - 18.42\right] \tag{4}$$

where $a_{LT,i,j}$ and $b_{LT,i,j}$ are the Landau-Teller coefficients. The Landau-Teller coefficients used in the present baseline model are taken from Park et al.[4] For the cases of present interest, the most significant $a_{LT,i,j}$ and $b_{LT,i,j}$ values are for $i = CO$ and $j = CO$, C, O, and N. While the Park et al. model applies the data of Millikan and White[51] for the CO–CO (i–j) coefficients, the data of Center[52] measured for CO–O is applied for the CO–C, CO–O, and CO–N coefficients. The $\tau_{v,i}^{MW}$ values resulting from Center's values for the CO–C, CO–O, and CO–N coefficients are many orders of magnitude smaller than if the Millikan and White correlation was applied. As a result of these small values, it is found that the contribution of $\tau_{v,i}^{MW}$ is small relative to $\tau_{v,i}^{P}$ for the cases of present interest.

The Park high temperature correction[25] to the relaxation time, $\tau_{v,i}^{P}$, is computed with the following formula:

$$\tau_{v,i}^{P} = \left(\frac{\pi m_i}{8kT_{tr}}\right)^{1/2} \frac{1}{\sigma_{v,i} N_{total}} \tag{5}$$

where $\sigma_{v,i}$ is the effective cross-section for vibrational relaxation. This term is represented as $\sigma_{v,i} = \sigma_{v,i}'(50,000/T_{tr})^2$ m^2. The $\sigma_{v,i}$ values applied for the present baseline model are taken from Park et al.[4] to be 3e-22, 1e-20, and 3e-21 m^2 for CO, CO_2, and N_2, respectively. The value for CO is the most important parameter in the present vibrational-translational relaxation model. This value was chosen as 3e-22 m^2 by Park et al. to fit the induction time data of Appleton et al.[39] However, applying the present shock capturing simulation to the Appleton et al. experiments does not reproduce the induction times computed by the shock fitted computation of Park et al., with the presently computed induction times being up to an order-of-magnitude smaller. Because the same thermochemical models are being applied in the present study as were applied by Park et al., the difference in computed induction times is likely a result of the different fluid mechanical treatment of the shock. Decreasing $\sigma_{v,CO}$ by one order-of-magnitude is found to result in good agreement between the present shock capturing simulations and the data of Appleton et al. In contrast to this proposed decrease in $\sigma_{v,CO}$, a recent study by Fujita[53] suggests an order of magnitude increase based on ab initio computations. Based on these conflicting values for $\sigma_{v,CO}$, a $\pm$ one order-of-magnitude uncertainty is assessed for this parameter. In the absence of other data, this uncertainty is applied for all $\sigma_{v,i}$ values.

The radiative flux sensitivity to $\sigma_{v,CO}'$ and $\sigma_{v,CO2}'$ was found to be less than $\pm 5\%$ for one order-of-magnitude changes in these parameters. For the other $\sigma_{v,i}'$ values the radiative flux sensitivity is less than $\pm 1\%$. It is found that for most cases a decrease in $\sigma_{v,i}'$ results in an increase in the radiative flux.

C. Radiative Flux Uncertainty Due to Flowfield Modeling Uncertainties

This subsection examines the possible upper and lower bounds of the radiative heating based on the parameter uncertainties identified in the previous two subsections. Note that all parametric uncertainties considered here are epistemic uncertainties, meaning those due to lack of knowledge. These epistemic uncertainties do not have an associated probability distribution, as they represent only the possible range of values for each parameter. This range of possible values for each parameter corresponds to a possible range of radiative flux values. The radiative flux uncertainty due to flowfield modeling parameters is therefore represented by the upper and lower radiative flux values possible given the parametric uncertainty bounds.[54] These upper and lower bounds are computed by adjusting the modeling parameters to their uncertainty bounds for maximum and minimum radiative heating. These two computations provide the upper and lower radiative heating uncertainty bounds due to flowfield uncertainties (this assumes that the radiative heating is a monatomic function of all parameters within their chosen uncertainty bounds, which has been observed to be true for all parameters considered here). These bounds are different than the sum of the individual sensitivities (presented in the previous 2 subsections) because of the nonlinear interaction between the flowfield kinetics and energy equations.

The previous two subsections reviewed the baseline chemical kinetic and vibrational energy relaxation models applied in the present study. The parameters in these models with the largest impact on radiative heating predictions were identified as the chemical kinetic rates ($k_{f,i}$) listed in Table 4 and the effective cross-section for vibrational relaxation ($\sigma'_{v,i}$). The sensitivity of the radiative heating to $\pm$ changes in these parameters was shown, as well as the possible uncertainty of these parameters based on theoretical and experimental data in the literature. In review, the chemical kinetic rate uncertainties are listed in Table 4 (all rates not listed in the table are assigned $\pm$ one order-of-magnitude uncertainties) while the $\sigma'_{v.i}$ uncertainties are assigned values of $\pm$ one order-of-magnitude. The sensitivity analysis presented in Table 3 indicates whether a positive or negative change in the chemical rate results in a positive or negative change in the radiative flux. In addition, it was found that decreasing $\sigma'_{v,i}$ increases the radiative flux.

The upper and lower bound computations result in the stagnation line temperature and radiative flux profiles presented in Figs. 19, 20, and 21 for the 5e-5, 1e-4, and 5e-4 kg/m^3 HIAD cases, respectively. The resulting uncertainty bounds are summarized in Table 5, where $\Delta q_{r,flow}$ represents the percent uncertainty in the baseline radiative flux (q_r) due to flowfield modeling parameters. The upper bound uncertainty is seen to be larger than 100% for the 5e-5 and 1e-4 kg/m^3 cases. This significant uncertainty is largely a result of the -75% CO dissociation rate uncertainty applied. Recall from Fig. 18(b) and Table 3 that a one order-of-magnitude decrease in this rate alone results in a similar radiative flux as the upper bound shown in Fig. 20(b).

The comparisons with EAST shock tube data presented in Section IV justified increasing the CO dissociation rate by more than an order-of-magnitude (a factor of 13) from the Park et al. heritage rate. The heritage rate is therefore below the -75% uncertainty bound applied to this new rate. If a lower uncertainty limit large enough to contain the heritage rate was applied, the upper uncertainty bounds listed in Table 3 would be greater than 200% for the 5e-5 and 1e-4 kg/m^3 cases. In this regard, the EAST measurements have allowed for a significant reduction in the baseline radiative flux uncertainty. It could be argued that the good comparisons with EAST measurements suggest that the -75% uncertainty on the CO dissociation rate should be reduced even more. However, the present authors believe that further measurements are required to adjust this uncertainty non-conservatively below the present -75% value.

Table 5: Radiative flux uncertainties due to flowfield modeling parameters

ρ_{inf} (kg/m^3)	q_r (W/cm^2)	$\Delta q_{r,flow}$ (%)
5e-5	9.38	+124, -36.9%
1e-4	14.3	+127, -32.9%
5e-4	40.2	+76.6, -9.20%

American Institute of Aeronautics and Astronautics

(a)

(b)
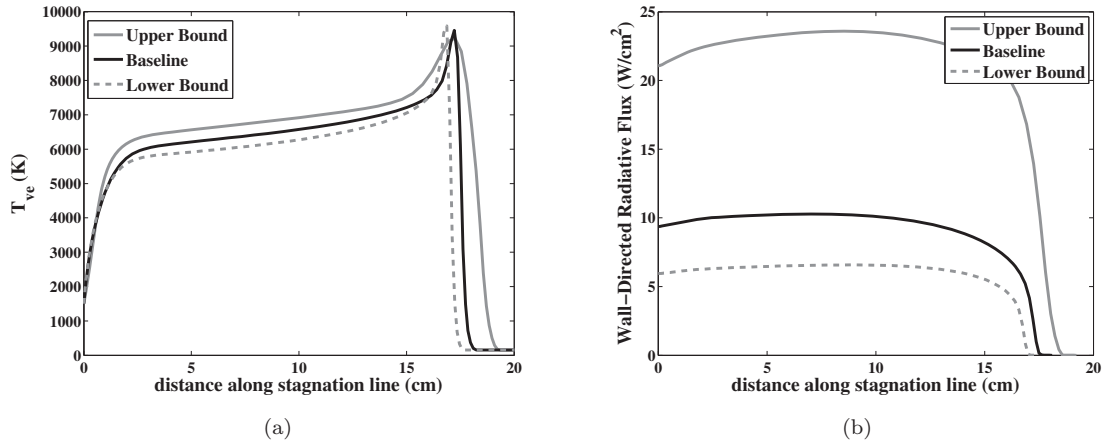
Figure 19: Stagnation line temperature and radiative flux profiles for upper and lower radiative heating bounds for the $\rho_{inf} = $ 5e-5 kg/m^3 case.

(a)

(b)
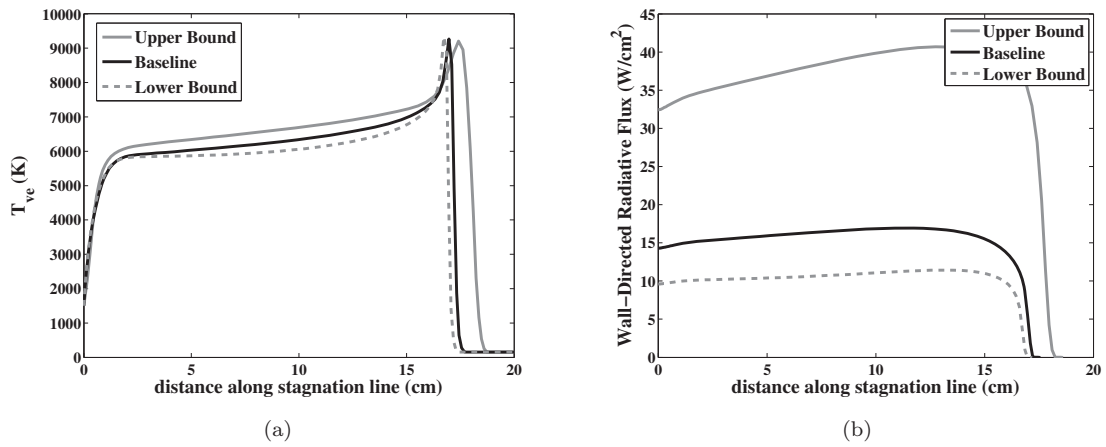
Figure 20: Stagnation line temperature and radiative flux profiles for upper and lower radiative heating bounds for the $\rho_{inf} = $ 1e-4 kg/m^3 case.

(a)

(b)
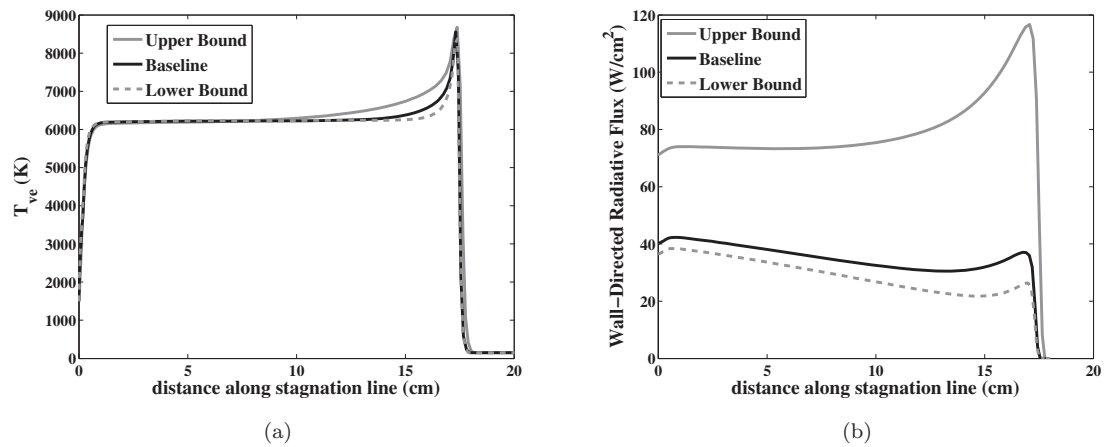
Figure 21: Stagnation line temperature and radiative flux profiles for upper and lower radiative heating bounds for the $\rho_{inf} = $ 5e-4 kg/m^3 case.

VI. Uncertainty Contribution due to Radiation Modeling Parameters

This section presents the baseline radiation model and its associated uncertainty, as was done in the previous section for the flowfield model (note that the baseline radiation model presented here was applied throughout the previous sections). Details of the radiative spectrum and non-Boltzmann modeling parameters applied in the present baseline model are presented in subsections A and B, respectively, along with the uncertainty for each parameter. A sensitivity analysis of the radiative flux is performed in subsection C to highlight the most important modeling parameters. Finally, in subsection D the radiative flux uncertainties due to these radiation modeling parameters are computed for the HIAD flight cases using the same approach applied in the previous section for the flowfield modeling parameters.

A. Spectrum Modeling

The molecular band systems treated in the present study, excluding those present in high temperature air, are listed in Table 6. The oscillator strengths presented by Babou et al.[12] are applied for all C_2 and CN band systems, along with the CO 4th Positive and CO Infrared systems. The oscillator strengths presented by da Silva and Dudeck[13] are applied for the remaining CO band systems.

Before assessing the oscillator strength uncertainty for the important CO 4th Positive band, it should be noted that the oscillator strengths for the vibrational bands with $\Delta v < -4$ are of primary interest (this is shown in Fig. 40 of Appendix A). This is because the radiative flux in the "blackbody limited" region of the spectrum, where $\Delta v > -4$, is relatively insensitive to the oscillator strengths, as indicated by Eqs. (23) and (25). The oscillator strengths from Babou et al.[12] applied in this work for CO 4th Positive are based on the ab initio electronic transition moment function (ETMF) of Kirby and Cooper.[55] Comparisons of this ETMF with experimental data, as well as with values proposed by other researchers,[56–59] has focused mostly on vibrational bands with $\Delta v > 0$. An exception to this is the work of Wallart et al.,[60] who shows that the ETMF of Kirby and Cooper compares better than that of Deleon[56] (which is applied by da Silva and Dudeck[13]) for vibrational bands with $\Delta v < -4$. In contrast to the findings of Wallart et al., comparisons with shock tube measurements by Brandis et al.[21] showed better agreement for these vibrational bands using the oscillator strengths of da Silva and Dudeck,[13] which predict nearly 30% less emission than the Babou et al. oscillator strengths. The variation in the oscillator strengths proposed by various researchers,[12, 13, 61] and the inconclusive validation of these values for $\Delta v < -4$ leads to the choice of a $\pm 40\%$ uncertainty for the oscillator strengths of the CO 4th Positive band system. A comparison between the results obtained by applying the Babou et al. and da Silva and Dudeck oscillator strengths is presented in Fig. 22 for the 6.71 km/s, 0.25 Torr EAST case considered previously in Fig. 10. The better agreement with measurements for the Babou et al. results in the equilibrium region (which is independent of the chemical rates tuned to agree in the nonequilibrium region) motivated the use of these values in the present baseline model instead of the da Silva values. As shown in Section IV, this good agreement in equilibrium is seen for all cases for both the CO 4th Positive and CN Violet band systems using the Babou et al. oscillator strengths.

(a) 165–215 nm (b) Distance = 8.0 cm
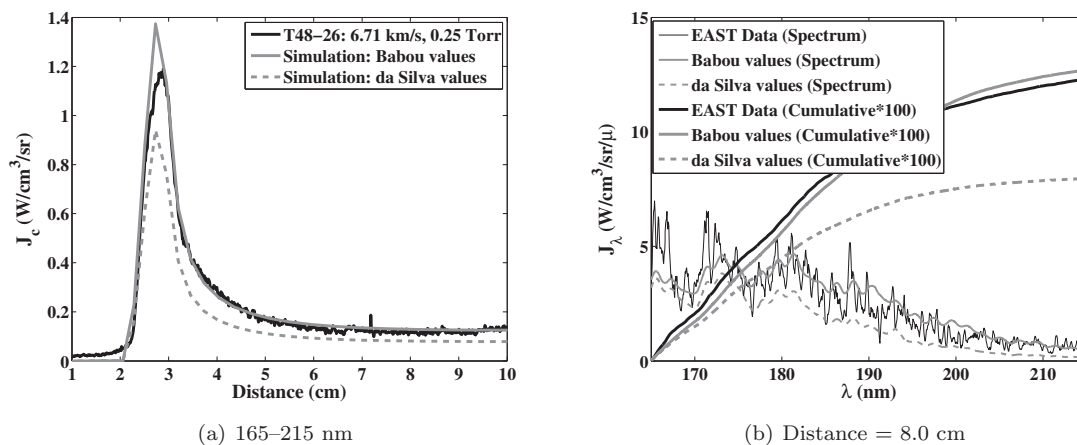
Figure 22: Comparison of nonequilibrium profiles for Test 48, Shot 26 at 6.71 km/s and 0.25 Torr.

Other than CO 4th Positive, the rest of the band systems for a Mars entry shock layer are optically thin, even CN Violet. This means the vibrational bands that contribute the most to the radiative flux, and are therefore of most interest in the uncertainty assessment, are those with $\Delta v = 0$. The oscillator strength uncertainties chosen for these band system are listed in Table 6. These values were obtained by comparing the values presented by the cited sources. The spectroscopic constants for the energy levels of molecules listed in this table were taken from Babou et al.[62] The oscillator strengths and spectroscopic constant for air band systems applied in this study are presented by Johnston.[18]

Table 6: Molecular band processes applied in the present study, excluding those present in high temperature air.

Molecule	Upper State – Lower State	Band Name	λ Range (nm)	+/- Uncertainty
CO	$A^1\Pi - X^1\Sigma^+$	4th Positive	$120 - 280$	40%[12, 13, 61]
CO	$b^3\Sigma^+ - a^3\Pi_r$	3rd Positive	$250 - 450$	50%[12, 13]
CO	$d^3\Delta_i - a^3\Pi_r$	Triplet	$320 - 2500$	50%[13]
CO	$a'^3\Sigma^+ - a^3\Pi_r$	Asundi	$370 - 2500$	50%[13]
CO	$B^1\Sigma^+ - A^1\Pi$	Angstrom	$400 - 700$	50%[13]
CO	$X^1\Sigma^+ - X^1\Sigma^+$	Infrared	$1200 - 7000$	50%[12, 13]
CN	$A^2\Pi_i - X^2\Sigma^+$	Red	$400 - 2800$	30%[12, 13, 61]
CN	$B^2\Sigma^+ - X^2\Sigma^+$	Violet	$300 - 550$	15%[12, 13, 61]
C_2	$d^3\Pi_g - a^3\Pi_u$	Swan	$390 - 1000$	50%[12, 13, 61]
C_2	$b^3\Sigma_g^- - a^3\Pi_u$	Ballik-Ramsay	$500 - 3000$	50%[12, 13, 63, 64]
C_2	$A^1\Pi_u - X^1\Sigma_g^+$	Phillips	$350 - 1200$	50%[12, 13]
C_2	$D^1\Sigma_u^+ - X^1\Sigma_g^+$	Mulliken	$200 - 250$	50%[12, 13]
C_2	$C^1\Pi_g - A^1\Pi_u$	Des.-D'Azam.	$280 - 700$	50%[12, 13]
C_2	$e^3\Pi_g - a^3\Pi_u$	Fox-Herzberg	$200 - 500$	50%[12, 13]
CO_2	$X^1\Sigma_g^+ - X^1\Sigma_g^+$	Infrared	$1700 - 25000$	50%
CO_2	$A^1B_2 - X^1\Sigma_g^+$	UV	$190 - 320$	100%

B.   Non-Boltzmann Modeling

The electronic state conservation equation, or Master equation, is written for each electronic state (j) of a molecule as the sum of the collisional (col) and radiative (rad) production rates:

$$\left(\frac{\partial N_j}{\partial t}\right) = \left(\frac{\partial N_j}{\partial t}\right)_{col} + \left(\frac{\partial N_j}{\partial t}\right)_{rad} \tag{6}$$

This equation is solved in the present study by making the quasi-steady state assumption,[25] which sets the left hand side of this equation equal to zero. The evaluation of the collisional and radiative production rates are discussed in the following two subsections.

1.   Treatment of Collisional Processes for Non-Boltzmann Modeling

The collisional component in Eq. (6) is computed using the flowfield number densities and given production rates as follows

$$\left(\frac{\partial N_j}{\partial t}\right)_{col} = \sum_{r=1}^{N_{col}} (\beta_{j,r} - \alpha_{j,r})(K_{f,r}N_iN_M - K_{b,r}N_jN_M) \tag{7}$$

where $\alpha_{j,r}$ and $\beta_{j,r}$ are the forward and backward stoichiometric coefficients for reaction r and electronic state j. For a reaction of the form

$$A(i) + M \leftrightarrow A(j) + M \tag{8}$$

the coefficients $\alpha_{j,r}$ and $\beta_{j,r}$ are equal to 0 and 1, respectively. In this reaction M is a heavy particle or electron and $A(i)$ and $A(j)$ are the lower and upper electronic states during the collision. The non-Boltzmann excitation rates applied in the present study will be listed in following paragraphs. The forward rates are

American Institute of Aeronautics and Astronautics

computed from provided coefficients, while the backward rates are computed for a reaction of the form of Eq. (8) as follows

$$K_{b,r} = K_{f,r} \frac{g_{e,i} exp(-\frac{hc}{kT_{ve}} E_{e,i})}{g_{e,j} exp(-\frac{hc}{kT_{ve}} E_{e,j})} \tag{9}$$

where g_e and E_e are the degeneracy and energy of the indicated electronic state.

The baseline excitation rate model applied in this work is an extension of the heavy-particle and electron-impact excitation rate models compiled by Park.[65, 66] The main differences between the present baseline model and Park's model are that the present model contains more recent data for some important rates and includes rates for C_2. These differences will be discussed in the following paragraphs. Note that the electron-impact and heavy-particle dissociation processes included by Park[65, 66] were found to be negligible for the present cases and are ignored. Table 7 presents the electronic levels treated in the present model for the three most significantly radiating molecules, CN, CO and C_2. The levels with the "(group)" label are actually combinations of closely spaced levels.

Table 7: Electronic levels treated in the present non-Boltzmann model.

i	Term	$E_{e,i}$	$g_{e,i}$
CN			
1	$X^2\Sigma^+$	0	2
2	$A^2\Pi$	9245	4
3	$B^2\Sigma^+$	25753	2
4	$a^4\Sigma^+$	32400	4
5	$D^2\Pi^+$	54486	4
CO			
1	$X^1\Sigma^+$	0	1
2	$a^3\Pi$	48687	6
3	$a'^3\Sigma^+$	55836	3
4	$d^3\Delta$	61120	6
5	$e^3\Sigma^-$ (group)	64230	6
6	$A^1\Pi$	65076	2
C_2			
1	$X^1\Sigma^+$ (group)	613.9	7
2	$b^3\Sigma^-$ (group)	7217	5
3	$c^3\Sigma^+$ (group)	11157.7	6
4	$d^3\Pi$	20022.5	6
5	$C^1\Pi$ (group)	31249.6	26

The heavy-particle impact excitation rates are computed from measured backward reaction (quenching) rates at 300 K ($K_{r,300}^{hp}$) using the approach presented by Park.[66] For optically allowed transitions, the forward reaction rate for the heavy-particle excitation from electronic state i to j is obtained from the following formula:

$$K_{f,ij}^{hp} = 4 \times 10^{-15} \frac{g_{e,j}}{g_{e,i}} \left(\frac{8k}{\pi\mu}\right)^{1/2} \left(\frac{1}{10,000}\right)^m T^{m+1/2} exp\left[-\frac{hc}{kT}(E_{e,j} - E_{e,i})\right] \tag{10}$$

where the exponent m is defined as

$$m = -0.657 \times log_{10}(7.70 \times 10^{20} K_{r,300}^{hp} \mu^{1/2}) \tag{11}$$

This equation assumes that the quenching cross section varies from the measured value at 300 K to the value of 4×10^{-15} cm^2 at 10,000 K. For optically forbidden transitions, the following formula is applied:

$$K_{f,ij}^{hp} = \frac{g_{e,j}}{g_{e,i}} K_{r,300}^{hp} \left(\frac{T}{300}\right)^{1/2} exp\left[-\frac{hc}{kT}(E_{e,j} - E_{e,i})\right] \tag{12}$$

Using Equations (10) and (12), each rate may be written in terms of constants A_{hp}, n_{hp}, and E_{hp} through the following expression

$$K_{f,ij}^{hp} = A_{hp} \left(\frac{T_a}{6000}\right)^{n_{hp}} exp(-E_{hp}/T_a) \tag{13}$$

American Institute of Aeronautics and Astronautics

where $T_a = (T_{ve}T_{tr})^{1/2}$. These constants are listed in Table 8 for each process. For brevity, the constants are not listed for rates that are dependent on the collision partner M. These rates may be found in Park.[66]

The source of each $K_{r,300}^{hp}$ value used to construct the rates listed in Table 8 are presented in the last column of this table. The rates labelled "Approx. (Park)" were computed by Park[66] using approximated $K_{r,300}^{hp}$ values. Those labelled "Approx. (Present)" were computed in the present work using $K_{r,300}^{hp}$ values assumed equal to the gas kinetic value of 1e-10 cm^3/s. It is seen in Table 8 that the rates compiled by Park[66] are used for all CN and CO rates, except for reactions 6 – 8, which represent transitions between the ground state of CO and the three highest excited states. Rates for these three reactions, which were not included in Park's final model, were taken from a review performed by Schofield.[67]

Reaction 8 is one of the most significant rates in the present non-Boltzmann model, as will be shown in the following subsection. This rate represents the excitation from the CO ground state to the upper level of the CO 4th Positive transition (A$^1\Pi$). The review by Schofield[67] shows that the proposed $K_{r,300}^{hp}$ values for this process vary by $\pm 50\%$. Applying Eq. (10) for this allowed transition, it is found that a 50% variation in $K_{r,300}^{hp}$ has a negligible impact on $K_{f,ij}^{hp}$ above 5000 K, which is the temperature range of present interest. This is a result of Eq. (10) assuming a fixed cross section of 4×10^{-15} cm^2 at 10,000 K, which causes the resulting $K_{f,ij}^{hp}$ above 5000 K to be insensitive to the chosen $K_{r,300}^{hp}$ values. The temperature dependence of $K_{f,ij}^{hp}$ assumed by Eq. (12) was based by Park on the limited temperature dependent data available for NO, N$_2$, and CO. The limited temperature dependent data for CO was obtained by Settersten et al.[68] for the B$^1\Sigma$ level (this level is not included in the present model) for temperatures up to 1000 K. This data is compared in Fig. 23 with the presently applied extrapolation. It is seen that assuming a constant cross section (which is presently applied for forbidden transitions) would compare just as well with the data. Figure 24 compares the rates for reaction 8 computed assuming the present variable cross section, assuming a constant cross section equal to its value at 300 K, and the rate presented by Zalogin.[16] This comparison shows a noticeable difference between the variable and constant cross section rates. It also shows that both rates are more than an order-of-magnitude greater than the Zalogin values. These observations suggest a $\pm$ one order-of-magnitude uncertainty for this rate. This same uncertainty will be applied to all rates in Table 8 that are non-"Approx.". For the "Approx." rates, no data is available for comparison and therefore a $\pm$ two orders of magnitude uncertainty is conservatively chosen.
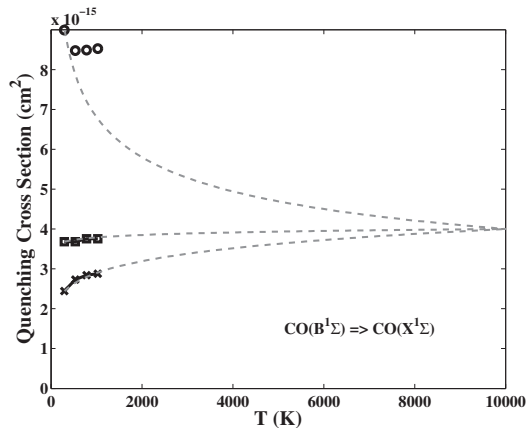
Figure 23: Quenching cross section temperature dependence for the CO B–X process (symbols represent measurements and dashed lines represent the present extrapolation).
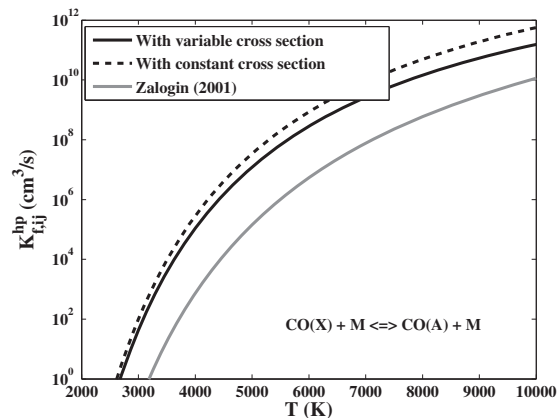
Figure 24: Excitation rate comparison for reaction 8.

The electron impact excitation rates applied in this baseline model are computed from electron impact excitation cross sections (σ_{el}) provided in the literature.[65] The forward reaction rate for electron-impact excitation from electronic state i to j is obtained from σ_{el} using the following formula:

$$K_{f,ij}^{el} = \frac{8\pi(hc)^2}{m_e^{1/2}} \left(\frac{1}{2\pi kT_e}\right)^{3/2} \int_{E^*}^{\infty} \sigma_{el} e^{-hcE/kT} E\, dE \qquad (14)$$

where E is energy (cm^{-1}) and E^* the threshold energy for the transition, equal to $E_{e,j} - E_{e,i}$. This equation is a simplified version of the equation suggested by Park.[65] It assumes that the Franck-Condon factors for a given lower level sum to 1.0. Compared to the significant uncertainties present for the σ_{el} values, the error

American Institute of Aeronautics and Astronautics

Table 8: Heavy-Particle impact excitation rates (cm^3/s) for non-Boltzmann modeling applied in the present study.

#	Reaction	A_{hp}	n_{hp}	E_{hp}	Source
1	$CN(X^2\Sigma^+) + M \leftrightarrow CN(A^2\Pi) + M$	M dependent			Park[66]
2	$CN(A^2\Pi) + M \leftrightarrow CN(B^2\Sigma^+) + M$	M dependent			Park[66]
3	$CN(B^2\Sigma^+) + M \leftrightarrow CN(a^4\Sigma^+) + M$	M dependent			Approx. (Park[66])
4	$CN(a^4\Sigma^+) + M \leftrightarrow CN(D^2\Pi^+) + M$	M dependent			Approx. (Park[66])
5	$CO(X^1\Sigma^+) + M \leftrightarrow CO(a^3\Pi) + M$	M dependent			Park[66]
6	$CO(X^1\Sigma^+) + M \leftrightarrow CO(a'^3\Sigma^+) + M$	5.20E-10	0.500	80370	Schofield[67]
7	$CO(X^1\Sigma^+) + M \leftrightarrow CO(d^3\Delta) + M$	2.61E-11	0.500	87975	Schofield[67]
8	$CO(X^1\Sigma^+) + M \leftrightarrow CO(A^1\Pi) + M$	2.52E-09	0.344	93669	Schofield[67]
9	$CO(a^3\Pi) + M \leftrightarrow CO(a'^3\Sigma^+) + M$	M dependent			Approx. (Park[66])
10	$CO(a'^3\Sigma^+) + M \leftrightarrow CO(d^3\Delta) + M$	M dependent			Approx. (Park[66])
11	$CO(d^3\Delta) + M \leftrightarrow CO(e^3\Sigma^-) + M$	M dependent			Approx. (Park[66])
12	$CO(e^3\Sigma^-) + M \leftrightarrow CO(A^1\Pi) + M$	8.78e-11	0.498	971	Approx. (Park[66])
13	$C_2(X^1\Sigma^+) + M \leftrightarrow C_2(b^3\Sigma^-) + M$	7.23e-10	0.773	9504.7	Approx. (Present)
14	$C_2(X^1\Sigma^+) + M \leftrightarrow C_2(c^3\Sigma^+) + M$	8.67e-10	0.773	15176.6	Approx. (Present)
15	$C_2(X^1\Sigma^+) + M \leftrightarrow C_2(d^3\Pi) + M$	7.49e-10	1.06	27927.7	Wang[69]
16	$C_2(X^1\Sigma^+) + M \leftrightarrow C_2(C^1\Pi) + M$	3.76e-09	0.773	44096.6	Approx. (Present)
17	$C_2(b^3\Sigma^-) + M \leftrightarrow C_2(c^3\Sigma^+) + M$	1.21e-09	0.773	5671.9	Approx. (Present)
18	$C_2(b^3\Sigma^-) + M \leftrightarrow C_2(d^3\Pi) + M$	1.21e-9	0.773	18423.0	Approx. (Present)
19	$C_2(b^3\Sigma^-) + M \leftrightarrow C_2(C^1\Pi) + M$	5.26e-09	0.773	34591.9	Approx. (Present)
20	$C_2(c^3\Sigma^+) + M \leftrightarrow C_2(d^3\Pi) + M$	1.01e-09	0.773	12751.1	Approx. (Present)
21	$C_2(c^3\Sigma^+) + M \leftrightarrow C_2(C^1\Pi) + M$	4.38e-09	0.773	28920.0	Approx. (Present)
22	$C_2(d^3\Pi) + M \leftrightarrow C_2(C^1\Pi) + M$	4.38e-09	0.773	16168.9	Approx. (Present)

introduced by this simplification are negligible. The resulting rate model is presented in Table 9, with each rate being represented through the following expression

$$K_{f,ij}^{el} = A_{el}T_{ve}{}^{n_{el}}exp(-E_{el}/T_{ve}) \tag{15}$$

The source of each cross section is listed in the table, where the abbreviation "Approx." indicates σ_{el} was approximated because no data was available in the literature. Park[65] discusses the choice of his approximate values for cases with no available data. The approximate cross sections chosen in the present work for C_2 are equal to the "formula of Huo" values listed by Park.[65]

The uncertainty associated with each rate is assessed by considering rates for which data from multiple sources is available. Comparisons for reactions 24 and 37 are compared in Figs. 25 and 26. As indicated in Table 9, the Harrison[70] and Park[65] rates shown in these figures are applied to reactions 24 and 37, respectively. It is seen that a $\pm$ one order-of-magnitude uncertainty would nearly cover the spread of proposed values. Similar comparisons are seen for other rates with multiple proposed values available. For the uncertainty analysis performed in subsection D, this $\pm$ one order-of-magnitude uncertainty will be applied for the non-"Approx." rates in Table 9. Since no data is available to assess the quality of the "Approx." rates, a $\pm$ two order of magnitude uncertainty will be applied.

American Institute of Aeronautics and Astronautics
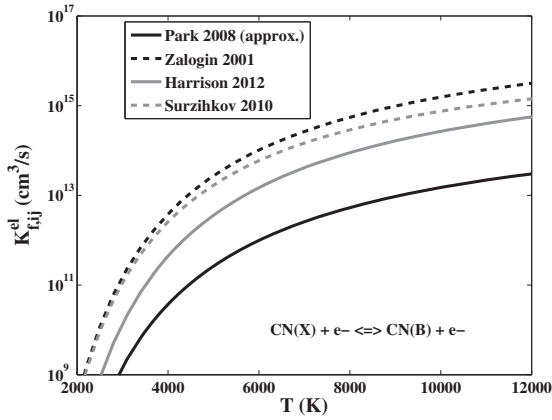
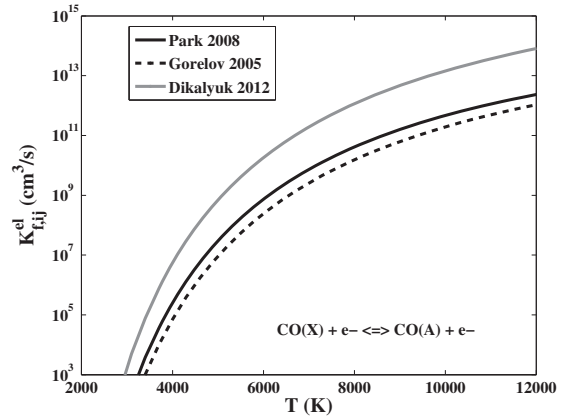Figure 25: Excitation rate comparison for reaction 24.

Figure 26: Excitation rate comparison for reaction 37.

Table 9: Electron-Impact excitation rates (cm^3/s) for non-Boltzmann modeling applied in the present study.

#	Reaction	A_{el}	n_{el}	E_{el}	Source
23	$CN(X^2\Sigma^+) + e^- \leftrightarrow CN(A^2\Pi) + e^-$	6.41e-09	0.20	18303	Harrison[70]
24	$CN(X^2\Sigma^+) + e^- \leftrightarrow CN(B^2\Sigma^+) + e^-$	6.83e-10	0.39	40428	Harrison[70]
25	$CN(X^2\Sigma^+) + e^- \leftrightarrow CN(a^4\Sigma^+) + e^-$	5.13e-11	0.35	47323	Approx. (Park[65])
26	$CN(X^2\Sigma^+) + e^- \leftrightarrow CN(D^2\Pi^+) + e^-$	4.07e-10	0.25	79368	Approx. (Park[65])
27	$CN(A^2\Pi) + e^- \leftrightarrow CN(B^2\Sigma^+) + e^-$	1.36e-04	-0.74	28030	Approx. (Park[65])
28	$CN(A^2\Pi) + e^- \leftrightarrow CN(a^4\Sigma^+) + e^-$	4.55e-04	-0.77	37548	Approx. (Park[65])
29	$CN(A^2\Pi) + e^- \leftrightarrow CN(D^2\Pi^+) + e^-$	1.22e-03	-0.82	69300	Approx. (Park[65])
30	$CN(B^2\Sigma^+) + e^- \leftrightarrow CN(a^4\Sigma^+) + e^-$	7.85e-05	-0.66	14148	Approx. (Park[65])
31	$CN(B^2\Sigma^+) + e^- \leftrightarrow CN(D^2\Pi^+) + e^-$	6.29e-04	-0.79	45559	Approx. (Park[65])
32	$CN(a^4\Sigma^+) + e^- \leftrightarrow CN(D^2\Pi^+) + e^-$	4.23e-04	-0.77	36015	Approx. (Park[65])
33	$CO(X^1\Sigma^+) + e^- \leftrightarrow CO(a^3\Pi) + e^-$	8.42e-11	0.28	80530	Riahi et al.[71]
34	$CO(X^1\Sigma^+) + e^- \leftrightarrow CO(a'^3\Sigma^+) + e^-$	1.82e-14	1.17	102434	Riahi et al.[71]
35	$CO(X^1\Sigma^+) + e^- \leftrightarrow CO(d^3\Delta) + e^-$	3.16e-12	0.66	114626	Riahi et al.[71]
36	$CO(X^1\Sigma^+) + e^- \leftrightarrow CO(e^3\Sigma^-) + e^-$	2.10e-14	1.17	113995	Riahi et al.[71]
37	$CO(X^1\Sigma^+) + e^- \leftrightarrow CO(A^1\Pi) + e^-$	3.82e-09	0.12	95850	Park[65]
38	$CO(a^3\Pi) + e^- \leftrightarrow CO(a'^3\Sigma^+) + e^-$	4.43e-8	-0.73	23456	Riahi et al.[71]
39	$CO(a^3\Pi) + e^- \leftrightarrow CO(d^3\Delta) + e^-$	7.74e-15	1.17	44552	Riahi et al.[71]
40	$CO(a^3\Pi) + e^- \leftrightarrow CO(e^3\Sigma^-) + e^-$	3.21e-15	1.27	44896	Riahi et al.[71]
41	$CO(a^3\Pi) + e^- \leftrightarrow CO(A^1\Pi) + e^-$	1.49e-05	-0.74	27860	Approx. (Park[65])
42	$CO(a'^3\Sigma^+) + e^- \leftrightarrow CO(d^3\Delta) + e^-$	2.53e-11	0.16	10611	Riahi et al.[71]
43	$CO(a'^3\Sigma^+) + e^- \leftrightarrow CO(e^3\Sigma^-) + e^-$	6.04e-13	0.61	11041	Riahi et al.[71]
44	$CO(a'^3\Sigma^+) + e^- \leftrightarrow CO(A^1\Pi) + e^-$	6.56e-06	-0.69	17750	Approx. (Park[65])
45	$CO(d^3\Delta) + e^- \leftrightarrow CO(e^3\Sigma^-) + e^-$	1.09e-10	1.66	10686	Riahi et al.[71]
46	$CO(d^3\Delta) + e^- \leftrightarrow CO(A^1\Pi) + e^-$	2.62e-06	-0.63	10570	Approx. (Park[65])
47	$CO(e^3\Sigma^-) + e^- \leftrightarrow CO(A^1\Pi) + e^-$	1.41e-06	-0.58	6971	Approx. (Park[65])
48	$C_2(X^1\Sigma^+) + e^- \leftrightarrow C_2(b^3\Sigma^-) + e^-$	5.25e-04	-0.876	12822.89	Approx. (Present)
49	$C_2(X^1\Sigma^+) + e^- \leftrightarrow C_2(c^3\Sigma^+) + e^-$	3.37e-05	-0.530	16676.24	Approx. (Present)
50	$C_2(X^1\Sigma^+) + e^- \leftrightarrow C_2(d^3\Pi) + e^-$	6.45e-08	-0.179	29932.77	Halmova[72]
51	$C_2(X^1\Sigma^+) + e^- \leftrightarrow C_2(C^1\Pi) + e^-$	1.00e-04	-0.396	45526.85	Approx. (Present)
52	$C_2(b^3\Sigma^-) + e^- \leftrightarrow C_2(c^3\Sigma^+) + e^-$	8.57e-03	-1.215	9893.11	Approx. (Present)
53	$C_2(b^3\Sigma^-) + e^- \leftrightarrow C_2(d^3\Pi) + e^-$	1.59e-05	-0.436	19375.79	Approx. (Present)
54	$C_2(b^3\Sigma^-) + e^- \leftrightarrow C_2(C^1\Pi) + e^-$	6.89e-05	-0.381	35594.37	Approx. (Present)
55	$C_2(c^3\Sigma^+) + e^- \leftrightarrow C_2(d^3\Pi) + e^-$	9.03e-05	-0.647	14918.32	Approx. (Present)
56	$C_2(c^3\Sigma^+) + e^- \leftrightarrow C_2(C^1\Pi) + e^-$	5.428e-05	-0.372	29691.92	Approx. (Present)
57	$C_2(d^3\Pi) + e^- \leftrightarrow C_2(C^1\Pi) + e^-$	1.09e-04	-0.495	17461.08	Approx. (Present)

American Institute of Aeronautics and Astronautics

2. Treatment of Radiative Processes for Non-Boltzmann Modeling

The evaluation of the radiative production rate for the Master equation, Eq. (6), is typically approximated as follows

$$\left(\frac{\partial N_j}{\partial t}\right)_{rad} = -\Lambda_{j,i} G_{em} N_j \tag{16}$$

where G_{em} is the radiative lifetime, which represents the depopulation of level j due to spontaneous emission to level i for a specified radiative transition, and $\Lambda_{j,i}$ is the escape factor, which represents the fraction of the emission that is not reabsorbed. Values of $\Lambda_{j,i}$ are usually assumed equal to 1.0 for an optically thin band system or a value close to zero for a completely optically thick band system. This approximate treatment simplifies the evaluation of Eq. 16 considerably because it removes its dependency on the non-local state of the gas. However, studies by Bose et al.[73] and Johnston et al.[74] for Titan entry and da Silva[75] and Sohn[76] for Earth entry have shown that assuming a constant $\Lambda_{j,i}$ leads to significant errors in the predicted radiative flux at certain conditions.

The present authors did not find any studies regarding the influence of $\Lambda_{j,i}$ for Mars entry radiation, and therefore a detailed study is included in Appendix B. This appendix presents the theoretical development and computational approach applied as well as detailed results for the $\rho_{inf} = 1e\text{-}4$ kg/m^3 case. It is found that the detailed treatment of $\Lambda_{j,i}$ leads to a significant increase in the CO 4th Positive emission. For example, the upper state number density of the CO 4th Positive band and radiative flux along the stagnation line are presented in Figs. 27 and 28 for cases with and without the detailed treatment of $\Lambda_{j,i}$. The "$\Lambda_{j,i}$ = Computed" result includes the detailed treatment of $\Lambda_{j,i}$ while the "$\Lambda_{j,i}$ = 1" result assumes optically thin band systems. The higher CO(A) number density seen in Fig. 27 for the $\Lambda_{j,i}$ = Computed case results in stronger CO 4th Positive emission and larger radiative flux values. A 50% increase in the total radiative flux reaching the surface is seen in Fig. 28 for the "$\Lambda_{j,i}$ = Computed" result. This significant increase in the radiative flux indicates that the detailed treatment of $\Lambda_{j,i}$ is required for accurate Mars entry radiation simulations. Consequently, all results presented in this paper, including the EAST simulations, include the detailed treatment of $\Lambda_{j,i}$.
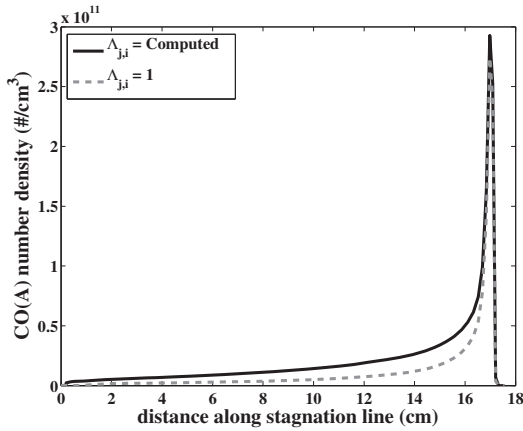
Figure 27: Stagnation line number density profiles of the CO(A$^1\Pi$) state for the $\rho_{inf} = 1e\text{-}4$ kg/m^3 case.
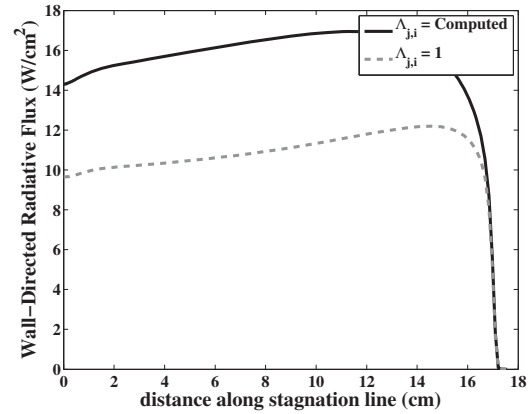
Figure 28: Stagnation line radiative flux profiles for the $\rho_{inf} = 1e\text{-}4$ kg/m^3 case.

C. Radiative Flux Sensitivity to Non-Boltzmann and Spectrum Modeling Parameters

The uncertainties in the spectrum and non-Boltzmann radiation modeling parameters were discussed in the previous two subsections. The sensitivity of the radiative flux for the 3 baseline cases (7 km/s at densities of 5e-5, 1e-4, and 5e-4 kg/m^3) to these parametric uncertainties is studied here. Assuming the baseline flowfield solution, a separate radiation calculation is made with each radiation modeling parameter adjusted to its upper and lower uncertainty bound (Note that for heavy-particle impact processes with multiple collision partners (M), the rates for all collision partners were adjusted together).

The resulting top 8 sensitivities are listed in Tables 10–12 for the 3 baseline cases. The listed sensitivities are the percent change from the baseline radiative heating for a positive ($+\Delta K_f$) or negative ($-\Delta K_f$) change in the specified parameter (the magnitude of the $\pm$ change in each parameter is listed in the column labelled "Uncertainty"). As expected, the top sensitivities for the relatively nonequilibrium 5e-5 kg/m^3 case are all

American Institute of Aeronautics and Astronautics

non-Boltzmann rates involving the radiating states of the CO 4th Positive and CN Violet band system. The sensitivity of greater than 100% seen for reaction 8 in Table 10 is significant. A discussion of the $\pm$ one order of magnitude uncertainty for this rate was discussed with Fig. 24. The large sensitivities to the other CO rates is a result of their ± 2 orders-of-magnitude uncertainty. As the free-stream density is increased, Tables 11 and 12 show the expected decrease in the radiative flux sensitivity to non-Boltzmann parameters and increase in the sensitivity to band oscillator strengths (indicated in the tables as the associated radiative process).

Table 10: Top 8 radiation modeling sensitivities for the ρ_{inf}=5e-5 kg/m^3 case.

#	Reaction	Uncertainty	+ΔK_f	-ΔK_f
8	$CO(X^1\Sigma^+) + M \leftrightarrow CO(A^1\Pi) + M$	1 om	112	-46.9
12	$CO(e^3\Sigma^-) + M \leftrightarrow CO(A^1\Pi) + M$	2 om	47.5	-8.00
41	$CO(a^3\Pi) + e^- \leftrightarrow CO(A^1\Pi) + e^-$	2 om	27.9	-0.41
46	$CO(d^3\Delta) + e^- \leftrightarrow CO(A^1\Pi) + e^-$	2 om	13.1	-5.00
2	$CN(A^2\Pi) + M \leftrightarrow CN(B^2\Sigma^+) + M$	1 om	6.18	-8.00
44	$CO(a'^3\Sigma^+) + e^- \leftrightarrow CO(A^1\Pi) + e^-$	2 om	11.9	-0.16
47	$CO(e^3\Sigma^-) + e^- \leftrightarrow CO(A^1\Pi) + e^-$	2 om	11.6	-0.14
27	$CN(A^2\Pi) + e^- \leftrightarrow CN(B^2\Sigma^+) + e^-$	2 om	9.47	-0.11

Table 11: Top 8 radiation modeling sensitivities for the ρ_{inf}=1e-4 kg/m^3 case.

#	Reaction	Uncertainty	+ΔK_f	-ΔK_f
8	$CO(X^1\Sigma^+) + M \leftrightarrow CO(A^1\Pi) + M$	1 om	47.2	-37.7
12	$CO(e^3\Sigma^-) + M \leftrightarrow CO(A^1\Pi) + M$	2 om	23.3	-5.10
41	$CO(a^3\Pi) + e^- \leftrightarrow CO(A^1\Pi) + e^-$	2 om	14.3	-0.25
2	$CN(A^2\Pi) + M \leftrightarrow CN(B^2\Sigma^+) + M$	1 om	3.85	-7.00
46	$CO(d^3\Delta) + e^- \leftrightarrow CO(A^1\Pi) + e^-$	2 om	6.73	-0.10
44	$CO(a'^3\Sigma^+) + e^- \leftrightarrow CO(A^1\Pi) + e^-$	2 om	6.54	-0.08
	$CO(A^1\Pi) \leftrightarrow CO(X^1\Sigma^+) + h\nu$	40%	1.69	-4.20
47	$CO(e^3\Sigma^-) + e^- \leftrightarrow CO(A^1\Pi) + e^-$	2 om	5.44	-0.07

Table 12: Top 8 radiation modeling sensitivities for the ρ_{inf}=5e-4 kg/m^3 case.

#	Reaction	Uncertainty	+ΔK_f	-ΔK_f
8	$CO(X^1\Sigma^+) + M \leftrightarrow CO(A^1\Pi) + M$	1 om	4.10	-7.86
	$CO(A^1\Pi) \leftrightarrow CO(X^1\Sigma^+) + h\nu$	40%	4.89	-6.58
	$CO(d^3\Delta) \leftrightarrow CO(a^3\Pi) + h\nu$	50%	3.24	-3.24
	$CN(B^2\Sigma^+) \leftrightarrow CN(X^2\Sigma^+) + h\nu$	15%	2.48	-2.54
2	$CN(A^2\Pi) + M \leftrightarrow CN(B^2\Sigma^+) + M$	1 om	1.22	-3.48
	$CO(X^1\Sigma^+) \leftrightarrow CO(X^1\Sigma^+) + h\nu$	50%	1.95	-2.15
12	$CO(e^3\Sigma^-) + M \leftrightarrow CO(A^1\Pi) + M$	2 om	2.06	-0.55
41	$CO(a^3\Pi) + e^- \leftrightarrow CO(A^1\Pi) + e^-$	2 om	1.42	-0.03

D. Radiative Flux Uncertainty Due to Non-Boltzmann and Spectrum Modeling Uncertainties

Similarly to Section III-C, where the upper and lower radiative heating bounds due to the uncertainty in *flowfield* modeling parameters were assessed, the present subsection assesses the upper and lower radiative heating bounds due to the uncertainty in *radiation* modeling parameters. The radiation modeling parametric uncertainties were discussed in parts A and B of the present section. To determine these upper and lower bounds, a computation is made with all radiation parameters adjusted to their uncertainty bound for maximum radiative heating and another computation is made with all radiation parameters adjusted to their uncertainty bound for minimum radiative heating. These bounds are different than the sum of the various sensitivity analyses because of the nonlinear interaction between the non-Boltzmann rates and the optical thickness of the CO 4th Positive band system.

American Institute of Aeronautics and Astronautics

The upper and lower bound computations result in the stagnation line $CO(A^1\Pi)$ number density and radiative flux profiles presented in Figs. 29–31 for the three baseline cases (note that flowfield uncertainties are not included in these computations so the flowfield is fixed for each case). Considering the $CO(A^1\Pi)$ number density figures, it is seen that the upper bound result approaches the Boltzmann result for all three cases (the Boltzmann curve is not plotted for the 5e-4 kg/m^3 case because it is indistinguishable from both the baseline and upper bound result). Note that in the boundary layer region below 2 cm, the influence of radiative absorption on the non-Boltzmann model causes the upper bound, baseline, and lower bound results (which all include non-Boltzmann computations) to have larger $CO(A^1\Pi)$ number densities than the Boltzmann result. The $CO(A^1\Pi)$ number densities for the lower limits are seen to deviate significantly more from the baseline values because there is no lower limit, such as the Boltzmann limit present for the upper bound.

Considering the radiative flux bounds in Figs. 29(b), 30(b), and 31(b), the expected larger spread of uncertainty bounds for the lower density case is seen. This behavior was also seen in the sensitivity analysis presented in the previous subsection. The uncertainty bounds presented in these figures are summarized in Table 13, where $\Delta q_{r,rad}$ represents the percent uncertainty in the baseline radiative flux (q_r) due to radiation modeling parameters. Comparing these values to the flowfield uncertainty bounds in Table 5, it is seen that the positive uncertainty bound ($\Delta q_{r,max}$) is lower for the radiation parameters than the flowfield parameters.

(a)

(b)

Figure 29: Stagnation line $CO(A^1\Pi)$ number density and radiative flux profiles for upper and lower radiative heating bounds due to radiation modeling parameters for the $\rho_{inf} = $ 5e-5 kg/m^3 case.

(a)

(b)

Figure 30: Stagnation line $CO(A^1\Pi)$ number density and radiative flux profiles for upper and lower radiative heating bounds due to radiation modeling parameters for the $\rho_{inf} = $ 1e-4 kg/m^3 case.

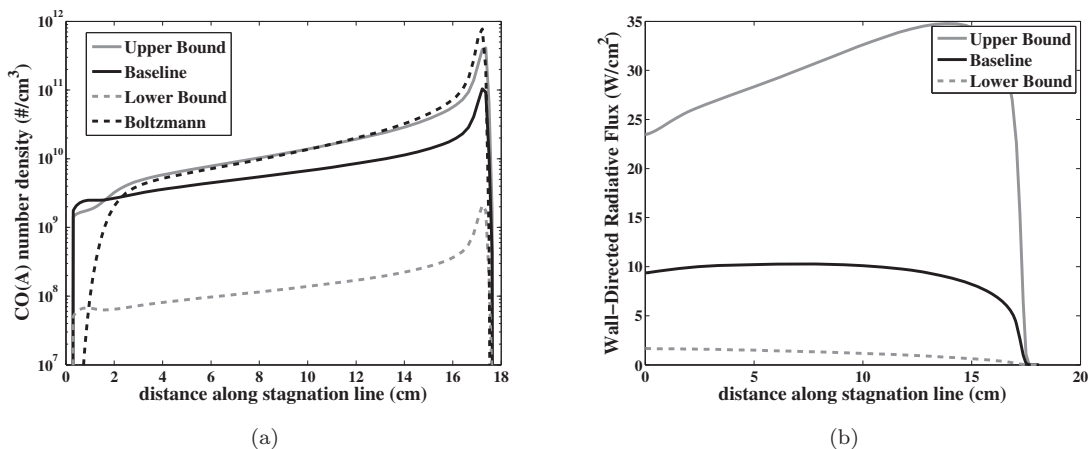American Institute of Aeronautics and Astronautics

(a)

(b)

Figure 31: Stagnation line CO($A^1\Pi$) number density and radiative flux profiles for upper and lower radiative heating bounds due to radiation modeling parameters for the ρ_{inf} = 5e-4 kg/m^3 case.
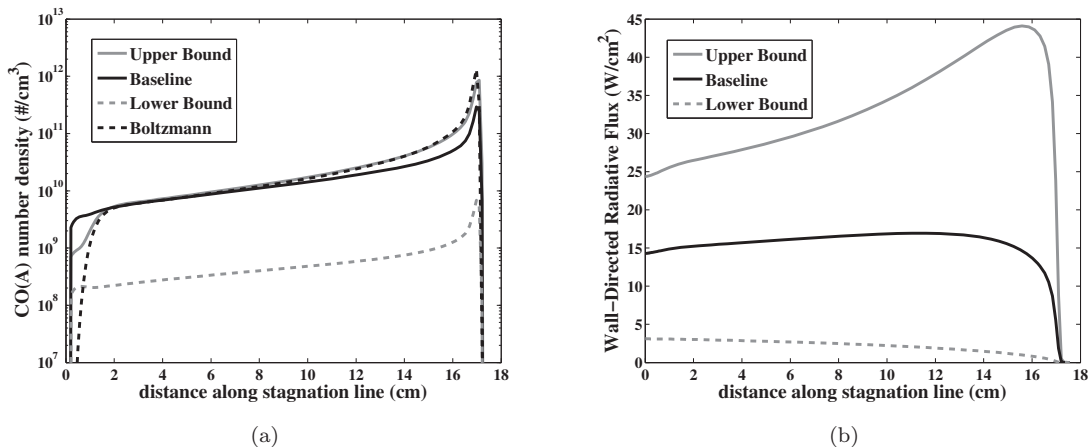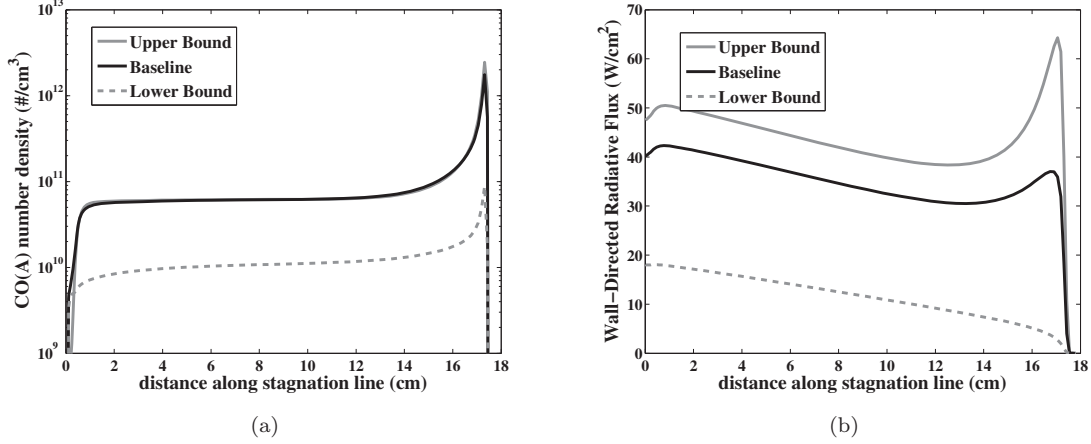
Table 13: Radiative flux uncertainties due to radiation modeling parameters.

ρ_{inf} (kg/m^3)	q_r (W/cm^2)	$\Delta q_{r,rad}$ (%)
5e-5	9.38	+150.5, -82.1%
1e-4	14.3	+70.5, -78.1%
5e-4	40.2	+18.2, -55.2%

VII.   Total Radiative Heating Uncertainty Assessment

The previous two sections assessed the radiative heating parametric uncertainty resulting separately from flowfield and radiation modeling. This separation of the parametric uncertainty is a consequence of the flowfield modeling parameters being inputs to the LAURA flowfield code and the radiation modeling parameters being inputs to the HARA radiation code. It was shown that the chemical kinetic rates provide the majority of the flowfield modeling uncertainty listed in Table 5, while the non-Boltzmann rates were shown to provide the majority of the radiation modeling uncertainty listed in Table 13. Because the non-Boltzmann rates were held fixed (as well as the other radiation parameters) while the chemical kinetic rates were tuned to match the EAST measurements, the chemical kinetic and non-Boltzmann rates are not independent of one another. As a result, the total uncertainty ($\Delta q_{r,total}$) is obtained using a root-sum squared (RSS) of the flowfield ($\Delta q_{r,flow}$) and radiation ($\Delta q_{r,rad}$) modeling uncertainties (if the flowfield and radiation parameters were independent, a simple sum would then be appropriate):

$$\Delta q_{r,total} = \sqrt{\Delta q_{r,flow}^2 + \Delta q_{r,rad}^2} \tag{17}$$

For the 7.0 km/s case considered throughout this paper, Table 14 presents $\Delta q_{r,total}$ and the associated components presented previously. The total uncertainty values are seen to range from +195% at the lowest density to +78.7% at the largest density. The dependency of these uncertainties on free-stream velocity is indicated in Tables 15 and 16, which present the baseline radiative flux and uncertainties for velocities of 7.7 and 6.3 km/s. These two velocities are seen to produce larger positive uncertainty values, which are a result of the larger flowfield uncertainty component ($\Delta q_{r,flow}$).

Also presented in Tables 14–16 are the stagnation point convective heating (q_c) values for each case. The super-catalytic and radiative equilibrium wall boundary conditions are applied for all flowfield computations. The super-catalytic assumption results in conservative convective heating values, but has a negligible influence on the radiative heating. These q_c values may be compared with the $q_{r,upper}$ values, which are equal to q_r increased by the positive $\Delta q_{r,total}$ component. It is seen that for the 7.0 and 7.7 km/s cases, the $q_{r,upper}$ values are nearly equal to or greater than the q_c values. This indicates the importance of the reducing the present radiative heating uncertainty.

Table 14: Baseline radiative flux and uncertainty values for a velocity of 7.0 km/s.

ρ_{inf} (kg/m^3)	q_c (W/cm^2)	q_r (W/cm^2)	$\Delta q_{r,flow}$ (%)	$\Delta q_{r,rad}$ (%)	$\Delta q_{r,total}$ (%)	$q_{r,upper}$ (W/cm^2)
5e-5	28.2	9.38	+124, -37%	+151, -82%	+195, -90%	27.7
1e-4	40.3	14.3	+127, -33%	+71, -78%	+145, -85%	35.0
5e-4	92.3	40.2	+77, -9.2%	+18, -55%	+79, -56%	72.0

Table 15: Baseline radiative flux and uncertainty values for a velocity of 7.7 km/s.

ρ_{inf} (kg/m^3)	q_c (W/cm^2)	q_r (W/cm^2)	$\Delta q_{r,flow}$ (%)	$\Delta q_{r,rad}$ (%)	$\Delta q_{r,total}$ (%)	$q_{r,upper}$ (W/cm^2)
5e-5	38.0	17.6	+172, -35%	+137, -79%	+220, -86%	56.3
1e-4	54.9	24.7	+149, -32%	+69, -75%	+164, -82%	65.2
5e-4	120	70.8	+58, -8.2%	+18, -54%	+61, -55%	114

From Tables 14–16, the appropriate uncertainty for a given trajectory may be assessed. The simplest approach would be to choose the uncertainty from these tables for the peak radiative heating point in the trajectory. However, the significant variation in these uncertainties with density prohibits the choice of a general uncertainty value for all cases. For cases out of the range of these tables, including other geometries, the uncertainty approach presented in this paper allows for the straightforward assessment of the radiative heating uncertainty.

VIII.   Application to Mars Pathfinder

The Mars Pathfinder vehicle successfully entered Mars in 1997.[77] The forebody heatshield consisted of a 70-degree half-angle sphere-cone with a 0.6638 m nose radius, 0.0662 m shoulder radius, and maximum diameter of 2.65 m. The free-stream conditions for three trajectory points near peak heating are presented in Table 17. The stagnation point convective heating assuming both a super catalytic ($q_{c,sc}$) and non-catalytic ($q_{c,nc}$) wall are presented. The baseline stagnation point radiative heating along with the flowfield and radiation modeling uncertainty components defined previously are presented for each trajectory point (only the upper limit uncertainty is presented for these cases). As in the previous section, the total radiative heating uncertainty is obtained using an RSS of the flowfield and radiation components. Finally, the upper-limit radiative heating ($q_{r,upper}$) is obtained, as discussed previously, by applying the total uncertainty to the baseline radiative heating. For the t=52 and 61 s cases, Figs. 32(a) and 33(a) present the stagnation line temperature and radiative flux profiles. It is seen that although the shock layer is a factor of 5 smaller than the previously studied HIAD cases, the radiative flux is of a similar magnitude because of the strong nonequilibrium emission contribution in both cases, which is independent of vehicle size or shock layer thickness.

A result of note in Table 17 is that if the actual convective heating is assumed to lie somewhere between the super- and non-catalytic values, then the radiative heating is a significant fraction of the heating at these trajectory points. This is especially true if the upper-limit radiative heating values are considered, which are actually larger than the non-catalytic convective heating for $t = 52$ and 61 s. This is shown in Figures. 32(a) and 33(a), which present the radiative and convective heating along the entire forebody. The $q_{r,upper}$ values are computed separately at each point on the surface. On the cone region of the surface, the

Table 16: Baseline radiative flux and uncertainty values for a velocity of 6.3 km/s.

ρ_{inf} (kg/m^3)	q_c (W/cm^2)	q_r (W/cm^2)	$\Delta q_{r,flow}$ (%)	$\Delta q_{r,rad}$ (%)	$\Delta q_{r,total}$ (%)	$q_{r,upper}$ (W/cm^2)
5e-5	21.0	1.51	+202, -22%	+167, -75%	+262, -78%	5.47
1e-4	29.2	2.67	+177, -24%	+79, -72%	+194, -75%	7.85
5e-4	66.0	8.98	+50, -6.1%	+18, -51%	+53, -52%	13.7

American Institute of Aeronautics and Astronautics

Table 17: Trajectory points near peak heating for the Mars Pathfinder vehicle.

t (s)	U_{inf} (m/s)	ρ_{inf} (kg/m^3)	$q_{c,sc}$ $(q_{c,nc})$ (W/cm^2)	q_r (W/cm^2)	$\Delta q_{r,flow}$ (%)	$\Delta q_{r,rad}$ (%)	$\Delta q_{r,total}$ (%)	$q_{r,upper}$ (W/cm^2)
52	7364	5.76e-5	86.6 (25.5)	13.6	+147%	+250%	+290%	53.0
61	6994	1.69e-4	121 (39.8)	18.7	+170%	+92%	+193%	54.8
66	6596	2.80e-4	125 (47.2)	10.8	+169%	+51%	+177%	29.9

convective heating decreases while the radiative heating maintains nearly a constant value. This implies a larger relative contribution from radiative heating in the cone region.
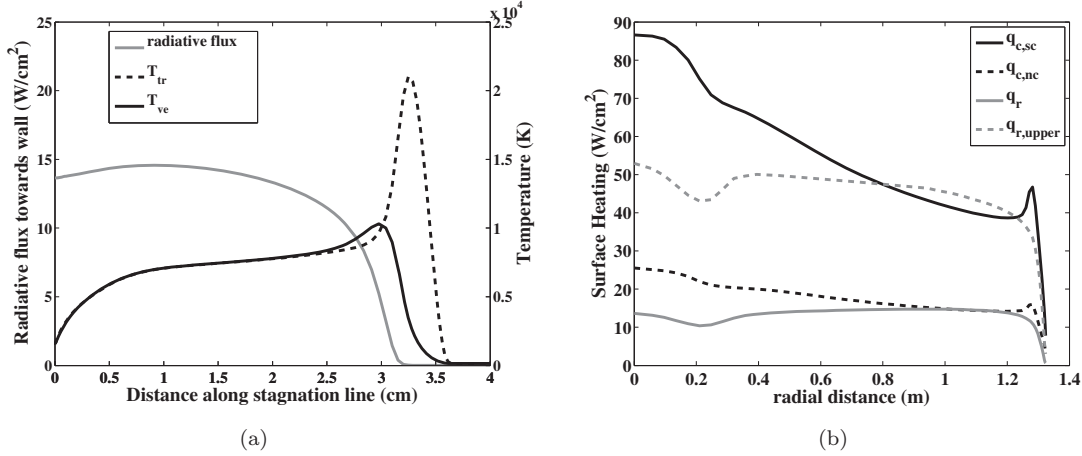

(a)   (b)

Figure 32: Stagnation line profiles and surface heating for t=52 s Pathfinder case.

(a)   (b)
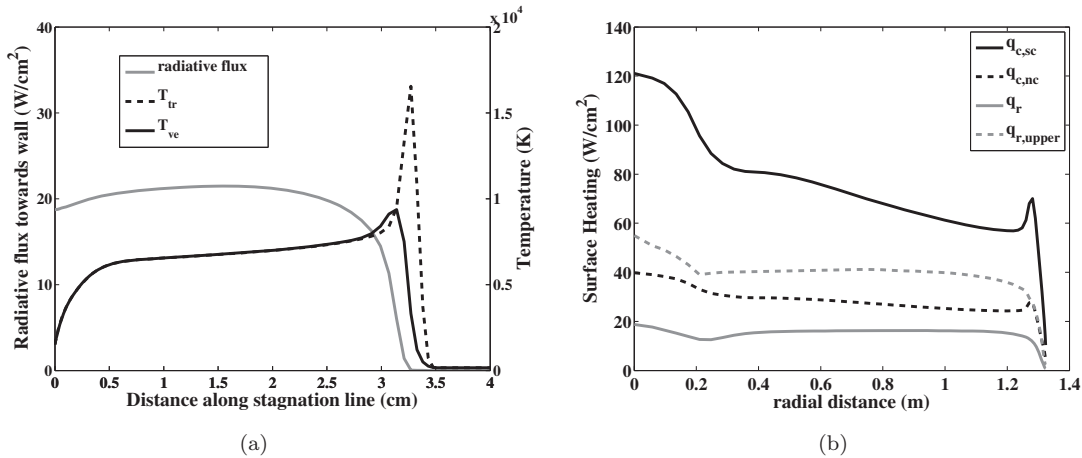
Figure 33: Stagnation line profiles and surface heating for t=61 s Pathfinder case.

Various pre- and post-flight aerothermal analyses of Pathfinder estimated the radiative heating using thermochemical equilibrium models.[78–80] As suggested by Figs. 1–3, these equilibrium models under-predicted the radiative heating relative to the present baseline model, with peak heating values of roughly 5 W/cm^2. These erroneously low values relative to the convective heating resulted in minimal attention for Pathfinder radiative heating simulations. The results of the present baseline model indicate that radiative heating was likely a larger contributor to the total heating for Pathfinder than previously thought. This conclusion is supported by recent studies by Surzikhov,[81,82] although these studies assumed a Boltzmann population of electronic states, which resulted in radiative heating a factor of 5 greater than the present (non-Boltzmann) model.

American Institute of Aeronautics and Astronautics

IX. Concluding Remarks

A model for simulating Mars entry radiative heating was developed and the uncertainty associated with this model was assessed. The developed model consists of chemical kinetic rates tuned to provide good agreement with recent EAST shock tube radiation measurements at 0.25 Torr, which contain nearly Boltzmann conditions for the strongly radiating CO and CN molecules. The most notable rate in this model was the CO dissociation rate, chosen as a factor of 13 greater than the commonly used Park rate. Applying a non-Boltzmann rate model based on recent values from the literature, the developed chemical kinetic rate model was then compared with measurements at 0.10 and 0.05 Torr, which contain strong non-Boltzmann emission. Good agreement was observed at these conditions to provide a level of validation for both the chemical kinetics and non-Boltzmann models. A sensitivity analysis was performed for the flowfield and radiation modeling parameters. For a range of free-stream conditions, the radiative flux was shown to be most sensitive to changes in the CO dissociation rate and CO heavy particle impact excitation rates. Using the uncertainty values chosen for each modeling parameter, radiative flux uncertainties due to the flowfield and radiation modeling parameters were computed. These uncertainties, due flowfield and radiation parameters, were combined using a root sum square to provide a total radiative heating uncertainty. The total radiative heating uncertainty was computed for a range of free-stream conditions and ranged from +262, -78% at the lowest free-stream velocity and density (6.3 km/s, 5e-5 kg/m^3) to +61, -55% at the highest free-stream velocity and density (7.7 km/s, 5e-4 kg/m^3). The developed model and uncertainty approach were applied to the Mars Pathfinder vehicle. A peak radiative heating of 18 W/cm^2 was predicted, which is significantly larger than the value of 5 W/cm^2 predicted in previous studies.

References

[1]Wright, M. J., Tang, C. Y., Edquist, K. T., Hollis, B. R., Krasa, P., and Campbell, C. A., "A Review of Aerothermal Modeling for Mars Entry Missions," , No. 2010-443, 2010.

[2]Ciancolo, A. M. D., Davis, J. L., Engelund, W. C., Komar, D. R., Queen, E. M., Samareh, J. A., Way, D. W., and Zhang, T. A., "Entry, Descent and Landing Systems Analysis Study: Phase 2 Report on Exploration Forward Systems," NASA TM 217055, 2010.

[3]Hollis, B. R. and Prabhu, D. K., "Assessment of Laminar, Convective Aeroheating Prediction Uncertainties for Mars Entry Vehicles," AIAA Paper 2011–3144, 2011.

[4]Park, C., Howe, J. T., Jaffe, R. L., and Candler, G. V., "Review of Chemical-Kinetic Problems for Future NASA Missions, II: Mars Entries," *Journal of Thermophysics and Heat Transfer*, Vol. 8, No. 1, 1994, pp. 9–23.

[5]Dikalyuk, A. S., Surzhikov, S. T., Shatlov, O. P., Kozlov, P. V., and Romaneko, Y. V., "Nonequilibrium Radiation Behind the Stron Shock Waves in Martian and Titan Atmospheres: Numerical Rebuilding of Experimental Data," AIAA Paper 2012–0795, Jan. 2012.

[6]Surzhikov, S. T., "Spectral Emissivity of Shock Waves in Martian and Titan Atmospheres," AIAA Paper 2010–4527, 2010.

[7]Anokhin, E. M., Ivanova, T. Y., Kudryavtsev, N. N., and Starikovskii, A. Y., "Dynamics of Radiation in a $CO:N_2$ Mixture behind Strong Shock Waves," *High Temperature*, Vol. 45, No. 6, 2007, pp. 733–739.

[8]Lee, E.-S., Park, C., and Chang, K.-S., "Shock-Tube Determination of CN Formation Rate in a $CO-N_2$ Mixture," *Journal of Thermophysics and Heat Transfer*, Vol. 21, No. 1, 2007, pp. 50–56.

[9]Boubert, P. and Rond, C., "Nonequilibrium Radiation in Shocked Martian Mixtures," *Journal of Thermophysics and Heat Transfer*, Vol. 24, No. 1, 2010, pp. 40–49.

[10]Grinstead, J., Wright, M., Bogdanoff, D., and Allen, G., "Shock Radiation Measurements for Mars Aerocapture Radiative Heating Analysis," *Journal of Thermophysics and Heat Transfer*, Vol. 23, No. 2, 2009, pp. 249–255.

[11]Cruden, B. A., Prabhu, D., Martinez, R., Lee, H., Bose, D., and Grinstead, J. H., "Absolute Radiation Measurements in Venus and Mars Entry Conditions," AIAA Paper 2010–4508, 2010.

[12]Babou, Y., Riviere, P., Perrin, M.-Y., and Soufiani, A., "Spectroscopic Data for the Prediction of Radiative Transfer in CO_2-N_2 Plasmas," *Journal of Quantitative Spectroscopy and Radiative Transfer*, Vol. 110, 2009, pp. 89–108.

[13]da Silva, M. L. and Dudeck, M., "Arrays of Radiative Transition Probabilities for CO_2-N_2 Plasmas," *Journal of Quantitative Spectroscopy and Radiative Transfer*, Vol. 102, 2006, pp. 348–386.

[14]Perrin, M.-Y., Riviere, P., and Soufiani, A., "Radiation Database for Earth and Mars Entries," RTO-EN-AVT 162, 2008.

[15]Gorelov, V. A., Kireev, A. Y., and Shilenkov, S. V., "Nonequilibrium Molecular Radiation Behind the Front of a Strong Shock Wave in the CO_2-N_2-O_2 Mixture," *Journal of Applied Mechanics and Technical Physics*, Vol. 46, No. 2, 2005, pp. 160–167.

[16]Zalogin, G. N., Kozlov, P. V., Kuznetsova, L. A., Losev, S. A., Makarov, V. N., Romanenko, Y. V., and Surzhikov, S. T., "Radiation Excited by Shock Waves in a CO_2-N_2-Ar Mixture: Experiment and Theory," *Technical Physics*, Vol. 46, No. 6, 2001, pp. 654–661.

[17]Mazaheri, A., Gnoffo, P. A., Johnston, C. O., and Kleb, B., "LAURA Users Manual," NASA TM 2010-216836, 2010.

[18]Johnston, C. O., Hollis, B. R., and Sutton, K., "Spectrum Modeling for Air Shock-Layer Radiation at Lunar-Return Conditions," *Journal of Spacecraft & Rockets*, Vol. 45, Sep.-Oct. 2008, pp. 865–878.

[19]Johnston, C. O., Hollis, B., and Sutton, K., "Non-Boltzmann Modeling for Air Shock Layers at Lunar Return Conditions," *Journal of Spacecraft & Rockets*, Vol. 45, Sep.-Oct. 2008, pp. 879–890.

[20]Johnston, C. O., Gnoffo, P. A., and Sutton, K., "Influence of Ablation on Radiative Heating for Earth Entry," *Journal of Spacecraft & Rockets*, Vol. 46, No. 3, 2009, pp. 481–491.

[21]Brandis, A. M., Johnston, C. O., Cruden, B. A., Prabhu, D. K., Wray, A. A., Liu, Y., Schwenke, D. W., and Bose, D., "Validation of CO 4th Positive Radiation for Mars Entry," AIAA Paper 2012–1145, Jan. 2012.

[22]Davies, W. O., "Carbon Dioxide Dissociation at 6000 and 11000 K," *Journal of Chemical Physics*, Vol. 43, No. 8, 1965, pp. 2809–2815.

[23]Nealy, J. E. and Haggard, K. V., "A Shock-Tube Study of Radiation Behind Shock Waves in CO_2 with Application to Venus Entry," Proceedings of the 9th international symposium on shock tubes and waves, 1973.

[24]Fujita, K., Yamada, T., and Ishii, N., "Impacts of Ablation Gas Kinetics on Hyperbolic Entry Radiative Heating," AIAA Paper 2006–1185, Jan. 2006.

[25]Park, C., *Nonequilibrium Hypersonic Aerothermodynamics*, Wiley, 1st ed., 1990.

[26]Bourdon, A. and Vervisch, P., "Study of Low-Presure Nitrogen Plasma Boundary Layer over a Metallic Plate," *Physics of Plasmas*, Vol. 4, No. 11, 1997, pp. 4144–4157.

[27]Ibragimova, L. B., "Recommended Rate Constants of $CO + O_2$ – Reversible – $CO_2 + O$ Reactions," *Khim. Fiz.*, Vol. 10, 1991, pp. 307–310.

[28]Gokcen, T., "N_2-CH_4-Ar Chemical Kinetic Model for Simulations of Atmospheric Entry to Titan," AIAA Paper 2004–2469, July 2004.

[29]Bose, D. and Candler, G. V., "Thermal Rate Constants of the O_2+N↔$NO + O$ Reaction based on the $^2A'$ and $^4A'$ Potential Energy Surfaces," *Journal of Chemical Physics*, Vol. 16, No. 107, 1997, pp. 6136–6145.

[30]Park, C., Jaffe, R. L., and Partridge, H., "Chemical-Kinetic Parameters of Hyperbolic Earth Entry," *Journal of Thermophysics and Heat Transfer*, Vol. 15, No. 1, 2001, pp. 76–90.

[31]Teulet, P., Gonzalez, J. J., Mercado-Cabrera, A., Cressault, Y., and Gleizes, A., "One-Dimensional Hydro-Kinetic Modeling of the Decaying Arc in Air-PA66-Copper Mixtures: I. Chemical Kinetics, Thermodynamics, Transport and Radiative Properties," *Journal of Physics D: Applied Physics*, Vol. 42, 2009, pp. 1–15.

[32]Park, C., "Review of Chemical-Kinetic Problems for Future NASA Missions, I: Earth Entries," *Journal of Thermophysics and Heat Transfer*, Vol. 7, No. 3, 1993, pp. 385–398.

[33]Brandis, A. M., *Experimental Study and Modeling of Non-Equilibrium Radiation During Titan and Martian Entry*, Ph.D. thesis, University of Queensland, 2009.

[34]Palmer, G., Prabhu, D., Brandis, A., and McIntyre, T. J., "Numerical Simulation of Radiation Measurements Taken in the X2 Facility for Mars and Titan Gas Mixtures," AIAA Paper 2011–3768, 2011.

[35]Oehlschlaeger, M. A., Davidson, D. F., Jeffries, J. B., and Hanson, R. K., "Carbon Dioxide Thermal Decomposition: Observation of Incubation," *Z. Phys. Chem.*, Vol. 219, 2005, pp. 555–567.

[36]Burmeister, M. and Roth, P., "ARAS Measurements on the Thermal Decomposition of CO_2 Behind Shock Waves," *AIAA Journal*, Vol. 28, No. 3, 1990, pp. 402–405.

[37]Jaffe, R., "Vibrational and Rotational Excitation and Dissociation of CO_2 Reexamined," AIAA Paper 2011-447, 2011.

[38]Hanson, R. K., "Shock-Tube Study of Carbon Monoxide Dissociation Kinetics," *Journal of Chemical Physics*, Vol. 60, No. 12, 1974, pp. 4970–4976.

[39]Appleton, J. P., Steinberg, M., and Liquornik, D. J., "Shock-Tube Study of Carbon Monoxide Dissociation Using Vacuum-Ultraviolet Absorption," *Journal of Chemical Physics*, Vol. 52, No. 5, 1970, pp. 2205–2221.

[40]Chakerian, C., "The Dissociation of Shock Heated Carbon Monoxide Studied by Two Wavelength Infrared Emission," *Shock Tube Research*, Imperial College, London, 1971.

[41]Mick, H.-J., Burmeister, M., and Roth, P., "Atomic Resonance Absorption Spectroscopy Measurements on High-Temperature CO Dissociation Kinetics," *AIAA Journal*, Vol. 31, No. 4, 1993, pp. 671–676.

[42]Wray, K. L. and Teare, J. D., "Shock-Tube Study of the Kinetics of Nitric Oxide at High Temperatures," *Journal of Chemical Physics*, Vol. 36, No. 10, 1962, pp. 2582–2596.

[43]Tsang, W. and Herron, J. T., "Chemical Kinetic Data Base for Propellant Combustion: I. Reactions Involving NO, NO_2, HNO, HNO_2, HCN, and N_2O," *The Journal of Physical and Chemical Reference Data*, Vol. 20, No. 4, 1991, pp. 609–663.

[44]Dean, A. J., Davidson, D. F., and Hanson, R. K., "A Shock Tube Study of Reactions of C Atoms with H_2 and O_2 Using Excimer Photolysis of C_3O_2 and C Atom Atomic Resonance Absorption Spectroscopy," *The Journal of Physical Chemistry*, Vol. 95, No. 1, 1991, pp. 183–191.

[45]Becker, K. H., Brockman, K. J., and Wiesen, P., "Spectroscopic identification of C(3P) atoms in halogenomethane + H flame systems and measurements of C(3P) reaction rate constants by two-photon laser-induced fluorescence," *J. Chem. Soc. Faraday Trans.*, Vol. 84, 1988, pp. 455–466.

[46]Dean, A. J., Hanson, R. K., and Bowman, C. G., "A Shock Tube Study of Reactions of C Atoms and CH with NO Including Product Channel Meaurements," *The Journal of Physical Chemistry*, Vol. 95, No. 8, 1991, pp. 3180–3189.

[47]Andersson, S., Markovic, N., and Nyman, G., "Computational Studies of the Kinetics of the C + NO and O + CN Reactions," *The Journal of Physical Chemistry*, Vol. 107, No. 28, 2003, pp. 5439–5447.

[48]Thielen, K. and Roth, P., "Resonance Absorption Measurements of N and O Atoms in High Temperature NO Dissociation and Formation Kinetics," *20th Symposium (International) on Combustion*, The Combustion Institute, Pittsburgh, Pa, 1984.

[49]Lee, J.-H., "Basic Governing Equations for the Flight Regimes of Aeroassisted Orbital Transfer Vehicles," AIAA Paper 1984–1729, 1984.

[50]Gnoffo, P. A., Gupta, R. N., and Shinn, J. L., "Conservation Equations and Physical Models for Hypersonic Air Flows in Thermal and Chemical Nonequilibrium," NASA TP 2867, Feb. 1989.

[51]Millikan, R. C. and White, D. R., "Systematics of Vibrational Relaxation," *Journal of Chemical Physics*, Vol. 39, No. 12, 1963, pp. 3209–3213.

[52]Center, R. E., "Vibrational Relaxation of CO by O Atoms," *Journal of Chemical Physics*, Vol. 58, No. 12, 1973, pp. 5230–5236.

[53]Fujita, K., "Vibrational Relaxation and Dissociation Kinetics of CO by CO–O Collisions," AIAA Paper 2008–3919, 2008.

[54]Johnston, C., Mazaheri, A., Gnoffo, P., Sutton, K., Brandis, A., Prabhu, D., and Bose, D., "Assessment of Radiative Heating Uncertainty for Hyperbolic Earth Entry," AIAA Paper 2011–3145, 2011.

[55]Kirby, K. and Cooper, D. L., "Theoretical Study of Low-Lying $^1\Sigma^+$ and $^1\Pi$ States of CO. II. Transition Dipole Moments, Oscillator Strengths, and Radiative Lifetimes," *Journal of Chemical Physics*, Vol. 90, No. 9, 1989, pp. 4895–4902.

[56]Deleon, R. L., "CO (A–X) Electric Dipole Transition Moment," *Journal of Chemical Physics*, Vol. 89, No. 1, 1988, pp. 20–24.

[57]Eidelsberg, M., Rostas, F., Breton, J., and Thieblemont, B., "Vibrational Band Oscillator Strengths and Dipole Transition Moment of the $A^1\Pi$–$X^1\Sigma$ System of CO," *Journal of Chemical Physics*, Vol. 96, No. 8, 1992, pp. 5585–5590.

[58]Federman, S. R., Menningen, K. L., Lee, W., and Stoll, J. B., "Relative Band Oscillator Strengths for Carbon Monoxide: $A^1\Pi$–$X^1\Sigma$ Transitions," *The Astrophysical Journal*, Vol. 477, 1997.

[59]Cooper, D. M. and Langhoff, S. R., "The Theoretical Study of Selected Singlet and Triplet States of the CO Molecule," *Journal of Chemical Physics*, Vol. 74, No. 2, 1981, pp. 1200–1210.

[60]Wallaart, H., Perrin, M.-Y., and Martin, J.-P., "The CO (A–X) Electric Dipole Transition Moment at Large Internuclear Distances," *Journal of Chemical Physics*, Vol. 101, No. 9, 1994, pp. 8264–8265.

[61]Rodio, J. and Hassan, H., "Spectroscopic Data and Model Predictions for Venus and Mars Atmospheres," AIAA Paper 2011–3949, 2011.

[62]Babou, Y., Riviere, P., Perrin, M.-Y., and Soufiani, A., "High Temperature and Nonequilibrium Partition Function and Thermodynamic Data of Diatomic Molecules," *International Journal of Thermophysics*, Vol. 30, 2009, pp. 416–438.

[63]Kokkin, D. L., Bacskay, G. B., and Schmidt, T. W., "Oscillator Strengths and Radiative Lifetimes for C_2: Swan, Ballik-Ramsay, Phillips, and $d^3\Pi_g$-$c^3\Sigma_u$," *Journal of Chemical Physics*, Vol. 126, No. 084302, 2007.

[64]Schmidt, T. W. and Bacskayt, G. B., "Oscillator Strengths of the Mulliken, Swan, Ballik-Ramsay, Phillips, and $d^3\Pi_g$-$c^3\Sigma_u$ Systems of C_2 Calculated by MRCI Methods Utilizing a Biorthogonal Transformation of CASSCF Orbitals," *Journal of Chemical Physics*, Vol. 127, No. 234310, 2007.

[65]Park, C., "Rate Parameters for Electronic Excitation of Diatomic Molecules I. Electron-Impact Processes," AIAA Paper 2008-1206, 2008.

[66]Park, C., "Rate Parameters for Electronic Excitation of Diatomic Molecules II. Heavy Particle-Impact Processes," AIAA Paper 2008-1446, 2008.

[67]Schofield, K., "Critically Evaluated Rate Constants for Gaseous Reactions of Several Electronically Excited Species," *Journal of Physical and Chemical Reference Data*, Vol. 8, No. 3, 1979, pp. 723–798.

[68]Settersten, T. B., Dreizler, A., and Fallow, R. L., "Temperature- and Species-Dependent Quenching of CO *B* probed by Two-Photon Laser-Induced Fluorescence using a Picosecond Laser," *Journal of Chemical Physics*, Vol. 117, No. 7, 2002, pp. 3173–3179.

[69]Wang, H., Zhu, Z., Zhang, S., Pei, L., and Chen, Y., "Time-Resolved Kinetic Studies on Quenching of C_2 $(d^3\Pi_g)$ by Alkanes and Substituted Methane Molecules," *Chemical Physics Letters*, Vol. 407, 2005.

[70]Harrison, S. and Tennyson, J., "Electron Collisions with the CN Radical: Bound States and Resonances," *Journal of Physics B: Atomic, Molecular and Optical Physics*, Vol. 45, 2012.

[71]Riahi, R., Teulet, P., Jaidane, N., and Gleizes, A., "Cross Section and Rate Coefficient Calculation for Electron Impact Excitation of the $a^3\Pi$, $a'^3\Sigma^+$, $d^3\Delta^-$ $e^3\Sigma^-$ and $D^1\Delta$ States of CO," *The European Physical Journal D*, Vol. 56, No. 1, 2010, pp. 67–72.

[72]Halmova, G., Gorfinkiel, J. D., and Tennyson, J., "Low-Energy Electron Collisions with C_2 Using the *R*-Matrix Method," *Journal of Physics B: Atomic, Molecular and Optical Physics*, Vol. 39, 2006.

[73]Bose, D., Wright, M. J., Raiche, G. A., Bogdanoff, D., and Allen, G. A., "Modeling and Experimental Validation of CN Radiation Behind a Strong Shock Wave," AIAA Paper 2005–0768, Jan. 2005.

[74]Johnston, C. O., Hollis, B. R., and Sutton, K., "Radiative Heating Methodology for the Huygens Probe," *Journal of Spacecraft & Rockets*, Vol. 44, No. 5, 2007, pp. 993–1002.

[75]da Silva, M. L., "An Adequate Treatment of Radiative Transfer in State-Resolved Nonequilibrium Flows," Centro de fisica de plasmas report, 2010.

[76]Sohn, I., Li, Z., and Levin, D. A., "Effect of Escape Factor to a Hypersonic Nonequilibrium Flow Implemented in DSMC Photon Monte Carlo Radiation," AIAA Paper 2011–0533, Jan. 2011.

[77]Willcockson, W. H., "Mars Pathfinder Heatshield Design and Flight Experience," *Journal of Spacecraft & Rockets*, Vol. 36, No. 3, 1999, pp. 374–379.

[78]Milos, F. S., Chen, Y.-K., Cogdon, W. M., and Thorton, J. M., "Mars Pathfinder Entry Temperature Data, Aerothermal Heating, and Heatshield Material Response," *Journal of Spacecraft & Rockets*, Vol. 36, No. 3, 1999, pp. 380–391.

[79]Gupta, R. N., Lee, K. P., and Scott, C. D., "Aerothermal Study of Mars Pathfinder Aeroshell," *Journal of Spacecraft & Rockets*, Vol. 33, No. 1, 1996, pp. 61–69.

[80]Chen, Y. K., Henline, W. D., and Tauber, M. E., "Mars Pathfinder Trajectory Based Heating and Ablation Calculations," *Journal of Spacecraft & Rockets*, Vol. 32, No. 2, 1995, pp. 225–230.

[81]Surzhikov, S. T. and Omaly, P., "Radiative Gas Dynamics of Martian Space Vehicles," AIAA Paper 2011–0452, Jan. 2011.

[82]Surzhikov, S. T., "Radiative-Convective Heat Transfer of a Spherically Shaped Space Vehicle in Carbon Dioxide," *High Temperature*, Vol. 49, No. 1, 2011, pp. 92–107.

[83]Johnston, C. O., "Improved Exponential Integral Approximation for Tangent-Slab Radiation Transport," *Journal of Thermophysics and Heat Transfer*, Vol. 24, No. 3, 2010, pp. 659–661.

Appendix

A. Simplified Mars Entry Radiation Transport

The radiative flux emitted from a Mars entry shock layer at conditions of present interest is the result of two fundamental regions through the shock layer. These two regions are identified as "A" and "B" in Fig. 34. Region A is the thin high temperature thermochemical nonequilibrium region directly behind the shock, while region B is the thicker, lower temperature region containing the remainder of the shock layer. From the flowfield shown in Fig. 34, temperatures and species number densities were chosen from two points representative of layers A and B. These properties are listed in Table 18 and will be used for examples throughout this section. The contribution of these two regions to the radiative flux reaching the surface may be studied by approximating both layers with constant properties. This allows an analytic solution to the radiative transport equations, which enables the influence of each layer on the radiative flux to be clearly interpreted.

Table 18: Properties for a simplified Mars entry shock layer at 7 km/s ($\Delta z_A = 1.5$ cm, $\Delta z_B = 15$ cm.)

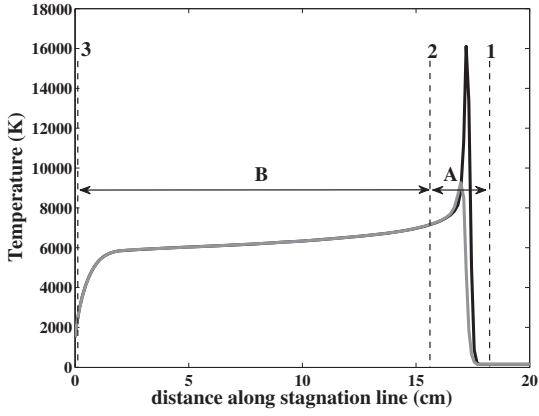| Layer	T_{tr}	T_{ve}	CO	CN	CO_2	N_2	O_2	NO	C	O	N	e^-
A	7836	8035	1.83e+16	2.95e+13	6.53e+13	4.82e+14	1.32e+14	6.51e+13	1.53e+15	2.11e+16	6.11e+14	1.78e+13
B	6280	6280	2.12e+16	1.77e+13	3.76e+11	1.11e+14	3.78e+12	1.81e+13	3.38e+15	2.80e+16	1.79e+15	2.97e+13

Figure 34: Identification of layers A and B for the 7 km/s, 1e-4 kg/m^3 case.
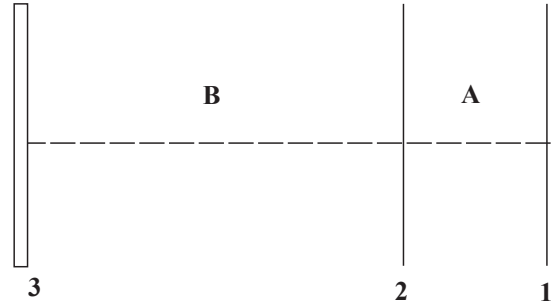

Figure 35: Schematic of layers A and B.

Following the schematic of Fig. 35, the radiative flux reaching the surface, or location 3, may be written in terms of the constant properties in layers A and B as follows:

$$q_{\nu,3} = q_{\nu,A}\Phi_B + q_{\nu,B} \tag{18}$$

where $q_{\nu,A}$ is the radiative flux emitted by layer A (at location 2) towards the wall, which is written as:

$$q_{\nu,A} = \pi\frac{j_{\nu,A}}{\kappa_{\nu,A}}\left(1 - \Phi_A\right) \tag{19}$$

and the absorption of flux as it moves through each layer, or transmissivity, is written as

$$\Phi_A = exp(-2\kappa_{\nu,A}\Delta z_A) \tag{20}$$

$$\Phi_B = exp(-2\kappa_{\nu,B}\Delta z_B) \tag{21}$$

These terms are dependent on the absorption coefficient (κ_ν) and thickness (Δz) of each layer. Figure 36 presents Φ_B for the current example and compares it with Φ_A. The CO 4th Positive band system, located between 6 and 10 eV, is seen to result in a significant reduction in Φ_B (note that atomic lines, which contribute less than 3%, are ignored for clarity in this appendix). The reduction is not as great for Φ_A because Δz_A is only 1.5 cm, while Δz_B is 15 cm. The radiative flux leaving layer A ($q_{\nu,A}$) and that reaching

American Institute of Aeronautics and Astronautics

the surface after passing through layer B ($q_{\nu,A}\Phi_B$) are presented in Fig. 37. It is seen that nearly 75% of flux emitted from layer A is absorbed in layer B. The Φ_B values below 0.1 seen in Fig. 36 are responsible for the nearly complete absorption of the flux above 8 eV, while both layers are seen to be optically thin below 6 eV.
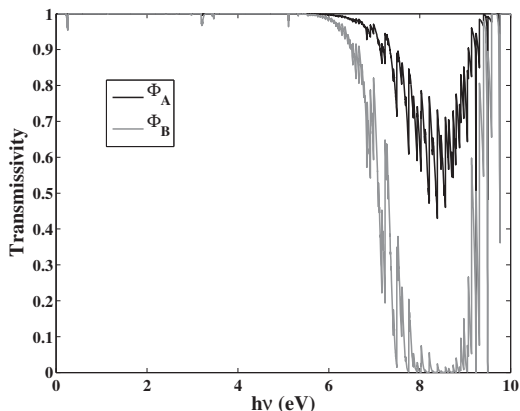

Figure 36: Spectral transmissivity of Layers A and B for the simplified shock layer defined in Table 18.
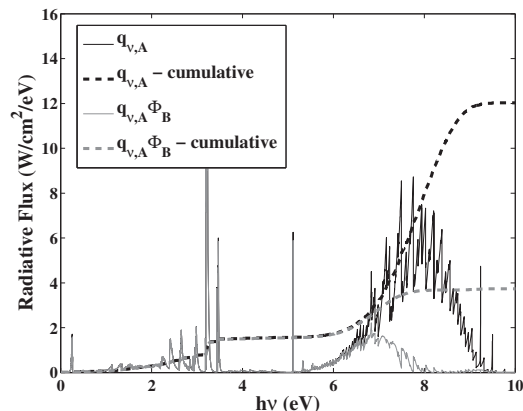

Figure 37: Radiative flux components for Layer A of the simplified shock layer defined in Table 18.

The emission from only layer B that reaches the surface is represented by $q_{\nu,B}$, which is written as

$$q_{\nu,B} = \pi \frac{j_{\nu,B}}{\kappa_{\nu,B}} \left(1 - \Phi_B\right) \tag{22}$$

Figure 38 presents $q_{\nu,B}$ for the current example. Comparing the spectrally integrated $q_{\nu,B}$ value of 6 W/cm^2 from this figure to the spectrally integrated $q_{\nu,A}$ value of 12 W/cm^2 from Fig. 37, it is apparent that the lower temperatures present in layer B result in significantly less emission than layer A (even considering the order of magnitude larger path length). However, Fig. 37 shows that the integrated $q_{\nu,A}$ value of 12 W/cm^2 is reduced to 3.8 W/cm^2 after passing through layer B. Therefore, the emission contributions of layers A and B to the total radiative flux reaching the surface is nearly equal, although the net flux from layer B is negative (-2.2 W/cm^2) as a result of its strong absorption. The total radiative flux reaching the surface ($q_{\nu,3}$) for this case is also presented in Fig. 38. As indicated by Eq. (18), this spectrum is the sum of the $q_{\nu,B}$ spectrum shown in this figure and the $q_{\nu,A}\Phi_B$ spectrum shown in Fig. 37.

A comparison of the radiative flux profile through the shock layer for the approximate 2-layer model and the actual shock layer is presented in Fig. 39. This figure shows that the 2-layer model captures the fundamental nature of the radiative environment, with the strong emission from layer A and strong absorption in layer B both clearly apparent in the actual flowfield result. The understanding of the radiative environment obtained in this appendix using the 2-layer model may therefore considered applicable to the actual flowfield radiation.
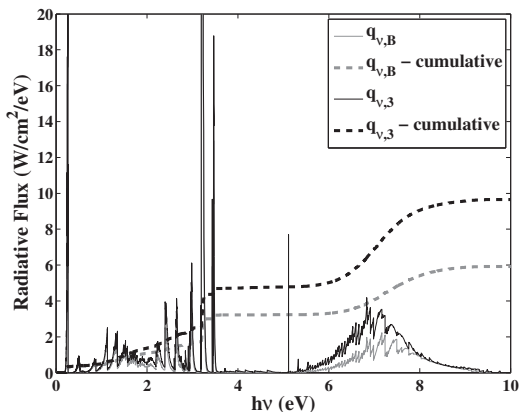

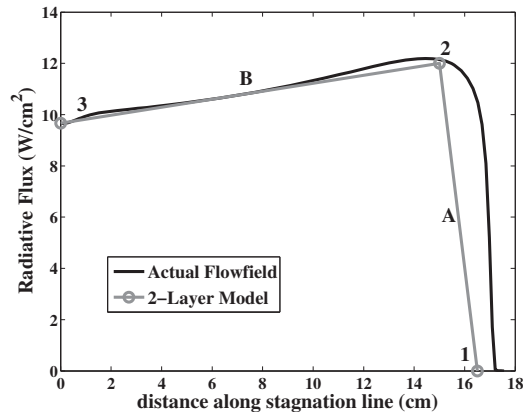Figure 38: Radiative flux components for the simplified shock layer defined in Table 18.

Figure 39: Wall directed radiative flux through the shock layer for the approximate 2-layer model and the actual shock layer.

American Institute of Aeronautics and Astronautics

The equations presented in this appendix are applicable to equilibrium and nonequilibrium radiation, or Boltzmann and Non-Boltzmann radiation, hence the Planck function is not used in these equations. Instead, the more general ratio of the emission (j_ν) and absorption (κ_ν) coefficients is applied. This term is of interest in the optically thick region of the spectrum, which is identified in Fig. 36 as the region above 8 eV where Φ_B is less than 0.1. In this spectral region, Eqs. (19) and (22) shows that the radiative flux reaching the surface reduces to the following form

$$q_{\nu,3} = \pi \frac{j_{\nu,B}}{\kappa_{\nu,B}} \tag{23}$$

For a spectral region dominated by a single band system, this equation may be written as

$$\frac{j_\nu}{\kappa_\nu} = \frac{2h\nu^3}{c^2} \frac{1}{\frac{N_i N_{j,boltz}}{N_j N_{i,boltz}} exp\left(\frac{h\nu}{kT_{ve}}\right) - 1} \tag{24}$$

which may be simplified to following for spectral regions above around 3 eV

$$\frac{j_\nu}{\kappa_\nu} = \left(\frac{N_j}{N_{j,boltz}}\right) \frac{2h\nu^3}{c^2} exp\left(-\frac{h\nu}{kT_{ve}}\right) = \left(\frac{N_j}{N_{j,boltz}}\right) B_\nu \tag{25}$$

where B_ν is the Planck function. Equations (23) and (25) show that the apparent "blackbody limited" region of a nonequilibrium spectrum is modified from its equilibrium radiation value, which is the Planck function, by the ratio of the radiating state number density to its Boltzmann value. These values are evaluated in layer B only. For the conditions listed in Table 18 for layer B, the value $N_j/N_{j,boltz}$ is equal to 0.29 for the CO 4th Positive band system. Figure 40 shows the reduction in the radiative flux below B_ν by this factor.
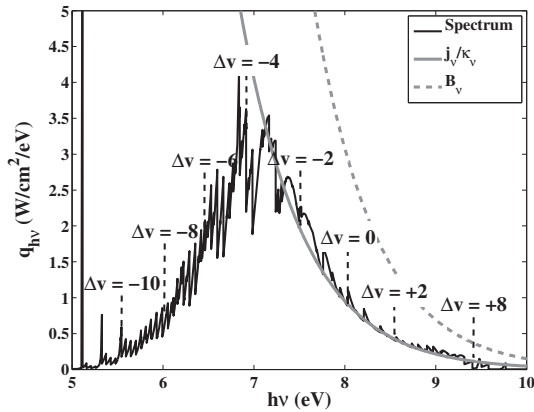

Figure 40: Example of "blackbody limiting" for non-Boltzmann radiation and identification of vibrational band heads.

B. Details of Treating Radiative Processes for Non-Boltzmann Modeling

The evaluation of the radiative production rate for the Master equation, Eq. (6), is the focus of this Appendix. The radiative production rate represents the change in the number density of an electronic level j due to radiative processes, which may be written as

$$\left(\frac{\partial N_j}{\partial t}\right)_{rad} = -\int_0^\infty \frac{4\pi j_{\nu,ij} - \kappa_{\nu,ij} \int_{4\pi} I_\nu d\Psi}{h\nu} d\nu \tag{26}$$

This equation assumes the electronic level j is the upper level of a radiative transition with a lower electronic level i. The absorption and emission coefficients due to this radiative transition only are written as $\kappa_{\nu,ij}$ and $j_{\nu,ij}$, respectively, while the radiative intensity I_ν is due to all radiative transitions occurring in the gas. The first term in this equation represents the depopulation of level j due to spontaneous emission to level i. This term, which will be divided by N_j (for future convenience) and referred to as G_{em}, may be evaluated as follows for a molecular band system

$$G_{em} = \frac{1}{N_j} \int_0^\infty \frac{4\pi j_{\nu,ij}}{h\nu} d\nu = \frac{Q_e}{Q_{int}} \sum_{v',v''} A_{v'v''} exp(-\frac{hc}{kT_v} E_{v'}) \frac{kT_r}{hcB_{v'}} \tag{27}$$

Note that G_{em} is dependent on only the local temperatures. This term is often referred to as the radiative lifetime, and has often been approximated using a constant value that ignores the temperature dependence in this equation. The internal partition function Q_{int} is written as

$$Q_{int} = \sum_j g_{e,j} exp(-\frac{hc}{kT_v}E_{e,j}) \sum_v exp(-\frac{hc}{kT_v}E_{v,j})\frac{kT_r}{hcB_{v,j}} \tag{28}$$

This term cannot be written as the product of an electronic, vibrational, and rotational partition function because the vibrational energy term $E_{v,j}$ is dependent on the electronic level j and the rotational energy term $B_{v,j}$ is dependent on both the vibrational quantum number v and j. As a result, the electronic partition function (Q_e) is in the numerator of Eq. (27) to divide out the Q_e component from Q_{int}.

The second term in Eq. (26) represents the repopulation of level j due to absorption in level i of the incoming radiative intensity resulting from the entire flowfield. This term will be referred to G_{ab} and written as

$$G_{ab} = \int_0^\infty \frac{\kappa_{\nu,ij}\int_{4\pi}I_\nu d\Psi}{h\nu}d\nu \tag{29}$$

Unlike G_{em}, which depends on only the local temperatures, this term depends on the incoming radiative intensity resulting from the entire flowfield. This dependence on the incoming radiative intensity complicates the evaluation of G_{ab} significantly. Not only does it require the solution of the radiative transport equations, but it also causes the solution of the Master equations to become an iterative process. Iterations are required because the incoming intensity at a point is dependent on the local emission, which is in turn dependent on the incoming intensity. The iteration procedure applied in this work will be discussed later.

The evaluation of the incoming intensity integral in G_{ab} is simplified in this work by making use of the tangent-slab approximation, which allows it to be written as

$$\int_{4\pi}I_\nu(z)d\Psi = 2\pi R_\nu(T_w)E_2[\tau_\nu(0,z)] + 2\pi\int_{s=0}^{s=z}j_\nu(s)\left|\frac{dE_2[\tau_\nu(s,z)]}{d\tau_\nu}\right|ds + 2\pi\int_{s=z}^{s=z_s}j_\nu(s)\left|\frac{dE_2[\tau_\nu(z,s)]}{d\tau_\nu}\right|ds \tag{30}$$

where z is the distance normal to the body (with the surface at $z = 0$ and the bow shock at $z = z_s$), E_2 is the second-order exponential integral, and τ_ν is the optical depth, which is defined as

$$\tau_\nu(s,z) = \int_s^z \kappa_\nu dz \tag{31}$$

Following Johnston,[83] the function E_2 may be closely approximated as follows

$$E_2(x) = 0.2653e^{-8.659x} + 0.7347e^{-1.624x} \tag{32}$$

which allows for the straightforward evaluation of Eq. (30) along rays normal to the body.

Using the definitions of G_{em} and G_{ab} in Eqs. (27) and (29), the change in the number density of an electronic level j due to radiative processes in Eq. (26) may be rewritten as

$$\left(\frac{\partial N_j}{\partial t}\right)_{rad} = -G_{em}N_j + G_{ab} \tag{33}$$

This form of the equation is applied to the Master equations for the solution of N_j at every point in the flowfield. Note that the G_{ab} term is moved to the right hand side of the system of linear equations that form the Master equations.

The iterative solution procedure for the Master equations is as follows. The first solution is obtained by assuming G_{ab} is equal to zero at every point along z. This provides initial values for N_j and allows the radiative emission and absorption coefficients to be computed. With these initial values, Eqs. (29) and (30) are evaluated to obtain G_{ab}. The Master equations are then solved again using this G_{ab} to obtain new values for N_j. The process is then repeated until the N_j values are not changed by more than 1% between iterations. This approach allows for a well converged solution in cases with strong absorption and weak emission, where G_{ab} is larger than $G_{em}N_j$. This is not the case if Eq. (33) is written in terms of an escape factor $(\Lambda_{j,i})$ as follows

$$\left(\frac{\partial N_j}{\partial t}\right)_{rad} = -\Lambda_{j,i}G_{em}N_j \tag{34}$$

where the escape factor is written as

$$\Lambda_{j,i} = 1 - \frac{G_{ab}}{G_{em}N_j^{m-1}} \tag{35}$$

and N_j^{m-1} represents the value of N_j from the previous iteration. This formulation does not converge for cases with strong absorption and weak emission because $\Lambda_{j,i}$ becomes negative, which changes the sign of Eq. (34) and causes the resulting N_j value to be negative.

Although it is not applied directly in solving the Master equation, it is convenient to present converged $\Lambda_{j,i}$ values to show the influence of absorption, or G_{ab}, on the computed electronic state number densities. From Eq. (35), it is seen that $\Lambda_{j,i}$ is equal to 1.0 for optically thin cases (meaning $G_{ab} = 0$), while it is equal to 0.0 for cases where emission and absorption balance each other exactly (meaning $G_{ab} = G_{em}N_j$). However, for regions with stronger absorption than emission ($G_{ab} > G_{em}N_j$), $\Lambda_{j,i}$ becomes negative. As indicated by Eq. (35), as G_{ab} becomes larger than $G_{em}N_j$ there is no limit to how negative $\Lambda_{j,i}$ may become. Large negative $\Lambda_{j,i}$ values are seen consistently in the boundary layer and free-stream, where the local emission is negligible (meaning G_{em} is small) but the intensity from the strongly emitting regions on the shock layer is absorbed locally (meaning G_{ab} is large)

The escape factor for the CO 4th Positive band system is presented in Fig. 41 along the stagnation line of the $\rho_{inf} = $ 1e-4 kg/m^3 case. A peak value of 0.9 is seen directly behind the shock, while further into the shock layer the escape factor decreases to negative values. The significant optical thickness of the CO 4th Positive band system is indicated by these values being noticeably less than 1.0 throughout the entire shock layer. The radiative lifetime, G_{em}, is also presented in Fig. 41. The temperature variation of the radiative lifetime, indicated in Eq. (27), is seen to be minimal, with values ranging from 2.2e+8 to 1.6e+8 s^{-1}. Note that these values are significantly different than the constant values of 3.3e+7, 1.0e+8 and 2.0e+9 s^{-1} applied by Gorelov,[15] Zalogin,[16] and Dikalyuk,[5] respectively. The impact of the radiative emission and absorption terms on the Master equation for the upper level of the CO 4th Positive band system, $CO(A^1\Pi)$, is shown in Fig. 42. The radiative emission component represents the first term in Eq. (33), while the radiative absorption component represents the second term. Radiative emission is seen to depopulate the $CO(A^1\Pi)$ level while radiative absorption and collisional excitation are seen to repopulate the level.
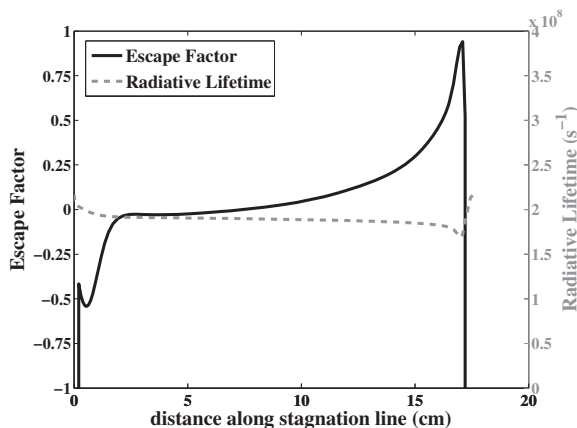

Figure 41: Stagnation line escape factor and radiative lifetime profiles of CO 4th Positive for the $\rho_{inf} = $ 1e-4 kg/m^3 case.
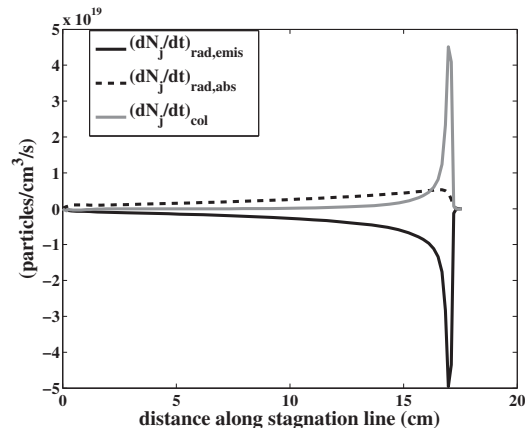
Figure 42: Stagnation line production rates profiles of the $CO(A^1\Pi)$ state for the $\rho_{inf} = $ 1e-4 kg/m^3 case.

For comparisons with the optically-thick CO 4th Positive case, Figs. 43 and 44 present the escape factor, radiative lifetime, and production rates for the nearly optically-thin CN Violet band. The escape factor is seen in Fig. 43 to be near 1.0 along most of the stagnation line, which indicates that the radiative absorption of this band system is small. The sharp decrease of the escape factor in the boundary layer (below 1.0 cm) is a result the low temperatures and weak emission in this region, as mentioned previously. The small contribution of radiative absorption on the Master equation is seen in Fig. 44, which shows a near zero contribution along the entire stagnation line. It is found that for all band systems in Mars entry shock layer, CO 4th Positive is the only band that contains enough absorption to noticeably influence the Master equation.
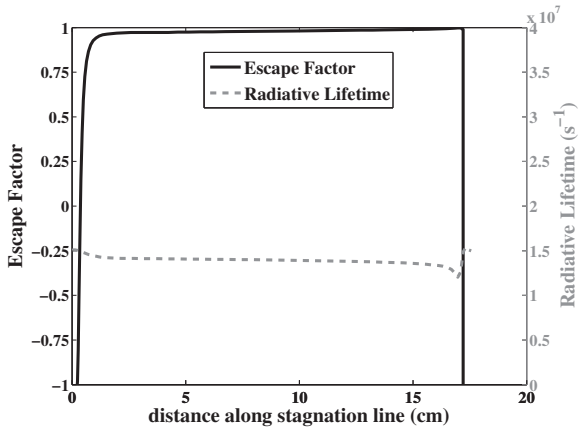
Figure 43: Stagnation line escape factor and radiative lifetime profiles of CN Violet for the $\rho_{inf} = $ 1e-4 kg/m^3 case.
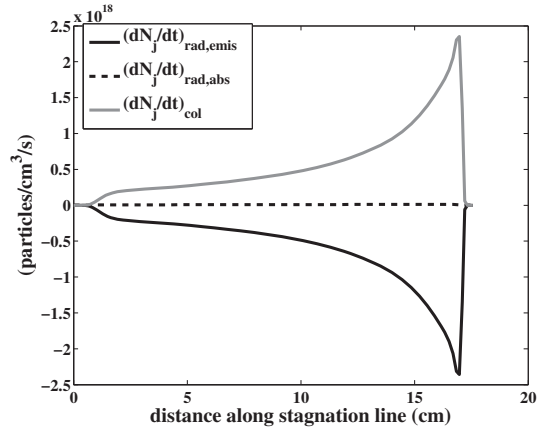

Figure 44: Stagnation line production rates profiles of the CN(B$^2\Sigma$) state for the $\rho_{inf} = $ 1e-4 kg/m^3 case.

American Institute of Aeronautics and Astronautics